ELSEVIER

Journal of Fluids and Structures 24 (2008) 34–57

JOURNAL OF FLUIDS AND STRUCTURES

www.elsevier.com/locate/jfs

# Numerical simulation of cross-flow around four cylinders in an in-line square configuration

K. Lam[a,*], W.Q. Gong[b], R.M.C. So[a]

[a]*Department of Mechanical Engineering, The Hong Kong Polytechnic University, Hung Hom, Kowloon, Hong Kong*
[b]*Xi'an Jiaotong University, Xi'an, PR China*

Received 15 October 2005; accepted 16 June 2007
Available online 24 September 2007

**Abstract**

Successful numerical simulations can reveal important flow characteristics and information which are extremely difficult to obtain experimentally. Two- and three-dimensional (3-D) numerical simulations of cross-flow around four cylinders in an in-line square configuration are performed using a finite-volume method. For 2-D studies, the Reynolds numbers (Re) are chosen to be $\mathrm{Re} = 100$ and 200 and the spacing ratio $L/D$ is set at 1.6, 2.5, 3.5, 4.0 and 5.0. For the 3-D investigation, the simulation is only performed at a $\mathrm{Re} = 200$, a spacing ratio $L/D = 4.0$ and an aspect ratio $H/D = 16$. The 2-D studies reveal three distinct flow patterns: (I) a stable shielding flow; (II) a wiggling shielding flow and (III) a vortex shedding flow. A transformation of the flow pattern from (I) to (II) at $\mathrm{Re} = 100$ will increase the amplitude of the maximum fluctuating pressure on the downstream cylinder surface by 4–12 times, while a transformation of the flow pattern from (II) to (III) will enhance the maximum fluctuating pressure amplitude by 2–3 times. There is a large discrepancy between 2-D simulation and flow visualization results at $L/D = 4.0$ and $\mathrm{Re} = 200$. A probable cause could be the strong 3-D effect at the ends of the cylinder at low $H/D$. It was found that, for an in-line square configuration at critical $L/D$ and when $H/D$ is lower than a certain value, 3-D effects are very significant at the ends of the cylinders. In such cases, a time-consuming 3-D numerical simulation will have to be performed if full replication of the flow phenomenon were to be achieved.


*Keywords:* Four cylinders; Flow pattern; Fluctuating pressure; Three-dimensionality

## 1. Introduction

Cross-flow around a group of cylinders is a very common phenomenon in engineering, such as flow around overhead cables, offshore structures, heat exchanger tube arrays, etc. The cross-flow-induced vibration might cause a reduction of equipment life and might even lead to the occurrence of severe accidents. Hence, it is necessary to understand the mechanism of flow-induced vibration and the associated fluid–structure interaction in order to improve the design of such equipment. Over the past 30 years, a great deal of attention has been focused on research on flow around cylindrical structures, especially on flow around one or two cylinders. Nevertheless, investigations of the flow past more than two cylinders are still relatively scarce because of the numerous parameters such as geometric parameters related to

*Corresponding author. Tel.: +852 2766 6649; fax: +852 2365 4703.
*E-mail address:* mmklam@polyu.edu.hk (K. Lam).

0889-9746/$ - see front matter © 2007 Elsevier Ltd. All rights reserved.
doi:10.1016/j.jfluidstructs.2007.06.003

cylinder arrangement, Reynolds number (Re), and boundary conditions that could affect the flow patterns. In the present study, the case of four cylinders in an in-line square configuration is investigated because a configuration with four equally spaced cylinders is a fundamental element in any tube array and offshore structures. It is a well-known fact that flow-induced vibration of cylinders is closely related to fluctuating pressure given rise by vortex shedding from the cylinder. Therefore, a numerical investigation of the relation between changes in flow pattern and the pressure, and hence the force characteristics of the cylinders in an in-line square configuration, at $Re = 100$ and 200 could enhance the understanding on the relation between vortex shedding and fluctuating pressure behaviour around the cylinder.

After conducting an extensive review and some experimental studies on flow interference between two circular cylinders, Zdravkovich (1987) proposed a classification for the flow pattern and flow interference between cylinders. He categorized the two cylinder arrangements into three types: side-by-side, tandem and staggered arrangements. For the side-by-side and tandem arrangements, a critical spacing is established by the minimum nondimensional distance between the two cylinders. At the critical spacing, the flow pattern around the cylinders undergoes a transformation. In the tandem configuration, if the cylinder spacing ratio ($L/D$) is larger than a critical value, the vortices shed from the upstream cylinder impinge on the downstream cylinder. Here, $D$ is the cylinder diameter and $L$ is the centre-to-centre distance between two cylinders. If the $L/D$ is less than a critical value, there is no vortex shedding from the upstream cylinder. The downstream cylinder is either shielded by the wake of the upstream cylinder, or a reattachment of the free shear layer from the upstream cylinder occurs. On the other hand, in the side-by-side configuration, a bistable feature of the flow behind the cylinders is observed under some conditions, which is an important flow characteristics often resulting in a large difference in force and Strouhal number (St) of the two cylinders. For the flow around four cylinders in an in-line square configuration, similar flow phenomena are expected to occur. It is anticipated that a numerical study could reveal in-depth details of the effects of $L/D$, $H/D$ (the aspect ratio where $H$ is the cylinder height) and Re on the transformation of flow patterns and their effects on the full-field velocity distribution, and on the pressure and force fluctuations, etc.

Some experimental studies on the flow around four cylinders in an in-line square configuration have been carried out. Sayers (1988) measured the lift and drag coefficient on a single cylinder in a group of four equally spaced cylinders in an open-jet wind tunnel at $L/D$ ranging from 1.1 to 5.0 and $Re = 3.0 \times 10^4$. A comparison with flow interference of a group of three cylinders shows that there exists similarly obtained data to form a basic code of design. Later, Sayers (1990) further determined the St of each cylinder in the same open-jet wind tunnel. The study indicated that at $L/D \geqslant 4.0$, St is equal to those for flow around a single isolated cylinder, while at $L/D < 4.0$, St varies across the wake. Lam and Lo (1992) had conducted a visualization study at $L/D$ ranging from 1.28 to 5.96, $H/D = 21.3$ and $Re = 2.1 \times 10^3$ and they summarized the flow characteristics into three flow patterns: (i) the downstream cylinder is shielded by the shear layers of the upstream cylinder (Fig. 1(a)), (ii) the free shear layers from the upstream cylinder is reattached onto the downstream cylinder (Fig. 1(b)) and (iii) the downstream cylinder is impinged by the vortices shed from the upstream cylinder (Fig. 1(c)). They also noticed a bistable feature of the flow behind the downstream cylinders corresponding to a narrow wake of high shedding frequency and a wide wake of low frequency at the high Re studied and below the $L/D$ case of Fig. 1(a). Lam and Fang (1995) studied experimentally the effects of flow interference of four-cylinder array on the mean pressure distribution and force coefficients of the cylinders. The $L/D$ investigated range from 1.26 to 5.80 with $H/D = 28.4$ and $Re = 12.8 \times 10^3$. Recently, Lam et al. (2003a) measured the mean and fluctuating lift and drag coefficients on the four cylinders at $L/D$ from 1.69 to 3.83 and $Re = 41.0 \times 10^3$, which give additional insight on the flow-induced forces. Further experimental investigations (Lam et al., 2001b, 2002, 2003b) using a DPIV (digital particle imaging velocimetry) method and an LIF (laser induced fluorescence) flow visualization technique confirmed the characteristics of the flow pattern observed around the four cylinders in an in-line square configuration. Based on these studies, it was possible to understand the flow physics and the relation between flow pattern transformation and $L/D$, the mean and fluctuating force and pressure characteristics on the cylinder. However,

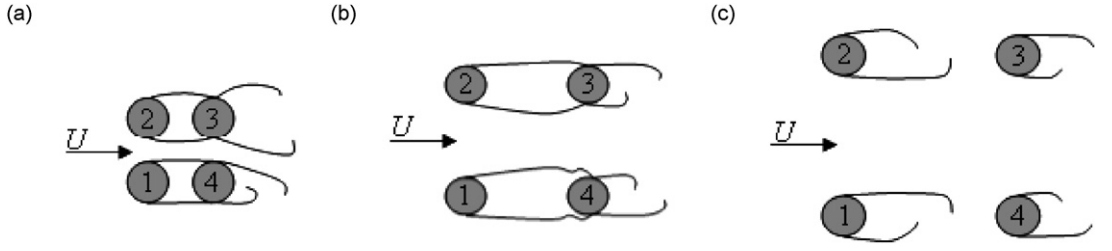


Fig. 1. Typical flow patterns around four cylinders in an in-line square configuration: (a) $L/D < 1.70$; (b) $1.70 < L/D < 3.94$; (c) $L/D > 3.94$.

inadequate understanding of the flow physics still exists. For example, the study on the mean and fluctuating lift and drag coefficients on four cylinders was limited to $1.69 \leqslant L/D \leqslant 3.83$; not sufficiently wide to cover the critical $L/D = 4.0$ (Lam et al., 2003a). The relation between flow pattern transformation and the fluctuating pressure distribution characteristics on the four-cylinder surfaces also has not been studied. Furthermore, these experimental results were limited to fairly high Re; little is known of the phenomena at low Re. One of the reasons could be due to measurement difficulties at low Re. Another reason is that most engineering applications occur at high Re. Applications at very low Re can be found in micro-devices, such as in MEMS devices (micro-electro-mechanical-systems) and cooling of fibres. Contrary to experimental studies, numerical simulation has obvious advantages in low-Re flow investigations. It can quickly provide flow information, such as the instantaneous full-field information of the velocity field, the vorticity field and the pressure field, which are very difficult to obtain experimentally.

Computational fluid dynamics (CFD) has become a powerful tool for solving complex fluid flow problems in the last decade and has been used to calculate the flow around single and multiple cylinders cover a wide range of Re, from 40 to $2.0 \times 10^6$ (Zdravkovich, 2003; Norberg, 2003). However, numerical studies of the flow around four cylinders in an in-line square configuration are relatively few. Among these studies are: Farrant et al. (2000) who used a cell boundary element method to simulate 2-D laminar flow at $\mathrm{Re} = 200$ and Lam et al. (2001a) who used a surface vorticity method to calculate 2-D flow at $\mathrm{Re} = 1.3 \times 10^3$ and $L/D = 1.5$. It was found that such behaviour as in-phase vortex shedding, anti-phase vortex shedding and synchronized vortex shedding, which are well-known characteristics for flow past two cylinders in side-by-side arrangements, were also present in this more complicated flow. Generally, the numerical methods were able to replicate the overall flow features and obtain good agreement with experimental results. However, if the 2-D simulation result of Farrant et al. (2000) was compared with the visualization results of Lam et al. (2001b, 2002, 2003a) at $L/D = 4.0$ and $\mathrm{Re} = 200$, an interesting observation could be deduced. The calculated flow pattern is almost completely different from that obtained from flow visualization experiments. In the simulation, mature vortex shedding occurs behind the upstream cylinder and impinges on the downstream cylinder surface, while visualization results show that the upstream free shear layers reattach onto the downstream cylinder at $L/D = 4.0$ and $\mathrm{Re} = 200$. Such a discrepancy in flow pattern could lead to a tremendous difference in the resultant velocity and pressure field, and the concomitant characteristics of the fluctuating forces, etc. Furthermore, in order to understand the physics and the associated effects of such flow patterns, it is necessary to develop numerical simulation of an in-line square configuration of four cylinders, where detailed information of the instantaneous full-field pressure and velocity distribution can be deduced.

The present work mainly concentrates on 2-D numerical simulations of the cross-flow around four cylinders in an in-line square configuration using a finite-volume method; a 3-D case study will also be carried out. For the 2-D study, $\mathrm{Re} = 100$ and 200 and $L/D = 1.6$, 2.5, 3.5, 4.0 and 5.0 are chosen. A major objective of this part of the study is to examine the relationship between flow pattern transformation and the pressure characteristics of the four cylinders. The effect of $L/D$ and Re on the flow pattern is first examined. For the 3-D simulation, a preliminary investigation at $\mathrm{Re} = 200$, $L/D = 4.0$ and $H/D = 16$ was performed. The reason behind the discrepancy between the 2-D calculation and flow visualization is discussed through the 3-D simulation. The analysis could give further insight into the cross-flow around four cylinders in an in-line square configuration, complementing previous experimental and numerical studies (Lam et al., 2001a, b, 2002, 2003a, b) of the flow around single and multiple cylinders.

## 2. Governing equations and numerical simulation

### 2.1. Numerical simulation scheme

The governing equations are the incompressible unsteady Navier–Stokes equations and the continuity equation, which can be written in dimensionless vector form as

$$\frac{\partial \mathbf{u}}{\partial t} + \mathbf{u} \bullet \nabla \mathbf{u} = -\nabla p + \frac{1}{\mathrm{Re}} \nabla^2 \mathbf{u}, \tag{1}$$

$$\nabla \bullet \mathbf{u} = 0, \tag{2}$$

where $\mathrm{Re} = U_\infty D/\nu$ is the Reynolds number, $U_\infty$ is the oncoming mainstream velocity, $\nu$ is the fluid kinematic viscosity, $\mathbf{u}$ is the nondimensional velocity vector in the Cartesian coordinate system $(x, y, z)$ with its three velocity components $u$, $v$, and $w$, and $p$ is the nondimensional static pressure. The calculation domain and the cylinder configuration are shown in Fig. 2, where $(x, y, z)$ denote the coordinates along the stream direction, the transverse

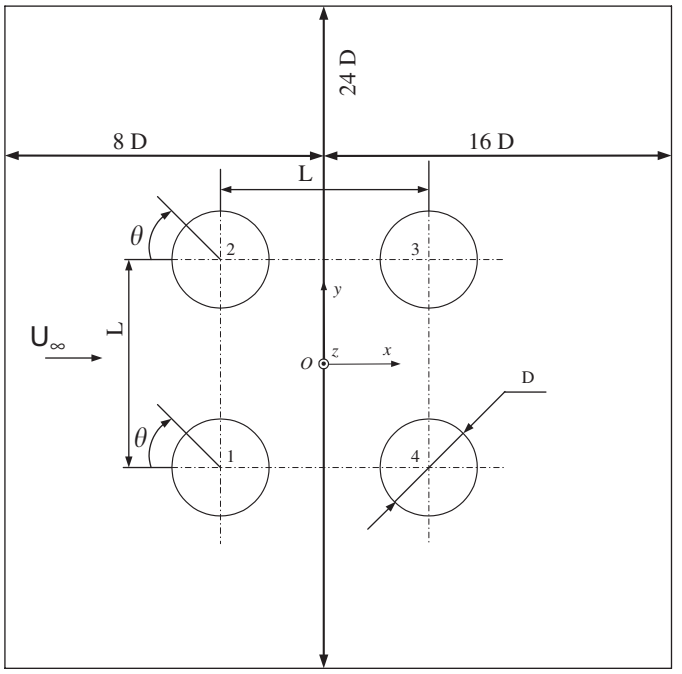


Fig. 2. Arrangement and computational domain for a four-cylinder array.

direction and the cylinder spanwise direction, respectively. The coordinate origin O (0, 0, 0) is located at the centre point of the four-cylinder arrangement. For the 2-D case, variation along the $z$-direction is not considered. For the 3-D case, the origin is placed on the cylinder bottom plane. All numerical simulations are carried out using the software package Fluent 6.1.22 on an IBM @ server P series 670 machine.

Farrant et al. (2000) indicated that a computational domain with $16D$ upstream, $14D$ downstream and $10D$ on either side of the cylinders could provide a better compromise between accuracy and computational costs for the flow around the cylinders. These values agree with the guidelines suggested by Tezduyar and Shih (1991) and Behr et al. (1995), where different mathematical models and numerical schemes were used. Based on flows past 2-D and 3-D simulation experience of the authors, a computational domain of $24D \times 24D \times 16D$ is chosen for the present simulation (Fig. 2) with an upstream distance of $8D$, a downstream distance of $16D$, and a distance of $12D$ on both sides of the cylinders. All these distances are measured from the coordinate origin. For the 3-D simulation, the height of the cylinder is $16D$. In order to save computer memory and time, only half of it is calculated in the computational domain. This is achieved by invoking a symmetry boundary condition at the central plane of the cylinders. The assumption is justified because recent numerical investigation by So et al. (2005) on flow-induced forces of a single cylinder in a cross-flow revealed that, even though the fluctuating force distributions exhibit full 3-D behaviour along the span, symmetry about the central plane does exist for $H/D$ ranging from 6 to 16.

A finite-volume method, based on the control volume technique, is used to obtain a solution of the general integral conservation form of the Navier–Stokes equation. The well-known SIMPLE technique is used to resolve the coupling between the pressure and the velocity fields. Discretization of the convective terms in the conservation equations is accomplished through a second-order accurate upwind differencing scheme because of its higher stability and veracity than the first-order upwind scheme used by other researchers (Shyy et al., 1992; Ni et al., 1998). The diffusion term is discretized using a central-difference technique, which is second-order accurate and is sufficient for the Re range of 100–200 investigated in the present study.

An unstructured mesh arrangement with hexahedral cell elements is specified for the flow domain. A dynamic solution-adaptive mesh refinement technique is used to accelerate the convergence process through the aid of the distribution gradient of parameter magnitude (Connell et al., 1993) as shown in Fig. 3. A second-order implicit forward discretization scheme is adopted for the time derivative term in order to accelerate the convergence process. The cell number is estimated to be about 80 000 for the 2-D simulations and 3 600 000 for the 3-D simulation at the Re and $L/D$ studied. The number of iterations at every time step is set at 15. The computing time for one time step is about 1 min for the 2-D cases and about 25 min for the 3-D simulation.

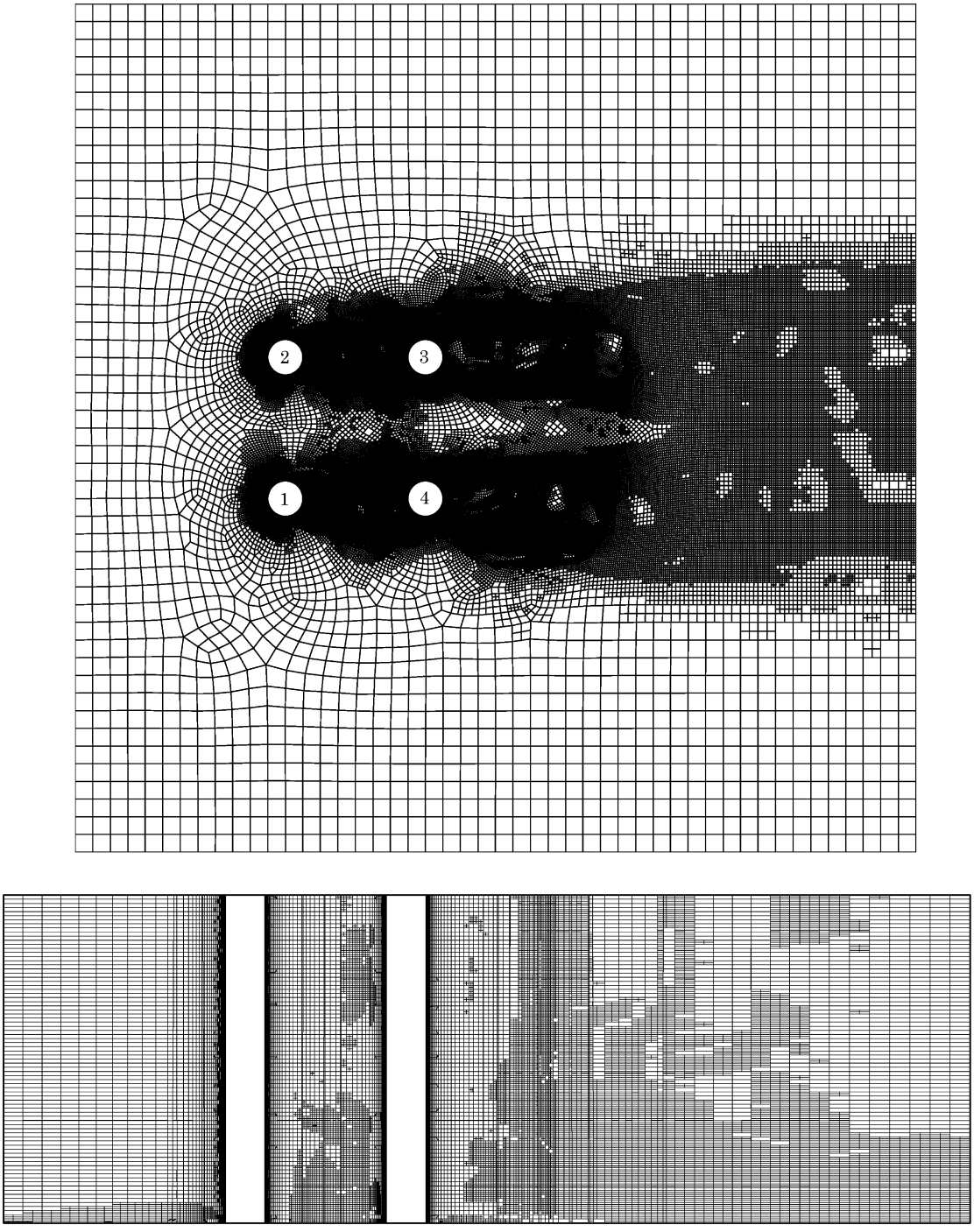


Fig. 3. Mesh distribution around four cylinders.

A uniform and constant mainstream velocity is specified at the inlet of the computational domain. Constant pressure at the other two sides and at the outlet is specified. No-slip boundary condition is invoked on all cylinder surfaces. The initial condition is assumed to be a uniform incoming flow. For the 3-D simulation, a symmetry condition on the cylinder central plane and a no-slip condition on one end-plane are stipulated.

The unsteady computation is terminated after the solution reaches periodic stability. Periodic stability is measured by the value of the calculated Strouhal number (St). If the change of St is less than 0.5% during 20 cycles, a stable periodic state is considered to have been reached. A similar measure has been used by Farrant et al. (2000).

### 2.2. Validity checking

Earlier simulations were carried out using boundary element or vortex methods, while recently, more efforts have been made to solve the unsteady Navier–Stokes equations directly for flows with $Re < 1000$ such as the studies of Liu et al. (2001), Meneghini et al. (2001), Jester and Kallinderis (2003). Breuer et al. (2000) investigated the confined flow around a cylinder with square cross-section mounted inside a plane channel at $Re = 300$ using two entirely different numerical techniques; a finite-volume method and a lattice Boltzmann automata method. Both numerical methods are of second-order accuracy in space and time. Accurate computations were carried out on grids with different resolutions. Velocity profiles and integral parameters such as drag coefficient, recirculation length and St were in excellent agreement with each other for the two methods. In the present study, a finite-volume method used to solve the unsteady Navier–Stokes equations is found to be a good approach to study complicated flows around four cylinders.

In order to validate the accuracy of the above described scheme, a group of 2-D and 3-D simulations of the flow around a single cylinder were carried out. The single cylinder centre coincides with the coordinate origin as shown in Fig. 2 with the other conditions remaining unchanged. Table 1 gives the St and force coefficients in the 2-D simulation for four mesh refinements and two nondimensional time steps $\Delta t$ ($\Delta t = Ut/D$) at $Re = 200$. In the dynamic solution-adaptive mesh refinement technique, the velocity gradient is used as a control threshold for refining mesh. For different schemes, the threshold lower and upper limits are different. This means that if the gradient on some mesh is lower than the lower limit, then the meshes will become coarser. On the other hand, if the gradient is higher than the upper limit, the relevant meshes will become finer and this leads to more computational time. As shown in Table 1, the two parameters (number of cells and $\Delta t$) have minor effect on the St and force coefficients in the attempted range. The error of St and $C_D$ is less than 2.55% and 3.33%, respectively, according to the results in Table 1. The 3-D simulation of the flow around a single cylinder is also performed using a similar scheme with symmetry boundary condition specified on the cylinder ends.

Comparing the results in Table 1 with those in Table 2, which also shows some previous simulation and experimental results of the flow around a single cylinder, it can be seen that all current results are very close to previous simulations or experimental results at similar Re range if the cell number exceeds 15 568 and $\Delta t = 0.01$ or 0.02. In these two tables, the mean drag coefficient is given by $\overline{C}_D$, the mean back pressure coefficient by $\overline{C}_{PB}$, and the root-mean-square values of the instantaneous coefficients by a prime. Table 2 shows that, even though the St value in the 2-D simulation is almost the same as the previously measured value [about 0.16 at $Re = 100$ (Jordan and Fromm, 1972); about 0.196 at $Re = 200$ (Williamson, 1991)], the St value 0.18 in a 3-D simulation [Persillon and Braza (1998) and present] is lower than a measured value of 0.196 at $Re = 200$. Furthermore, the $\overline{C}_D$ value 1.274 in the 3-D simulation at $Re = 200$ is less than the measured value while the $\overline{C}_D$ value 1.32 in the 2-D simulation is greater than the experimental value 1.30 except that reported by Meneghini et al. (2001). Even then, present and previous St and $\overline{C}_D$ as a whole are very close to the experimental results. Thus, to reduce the simulation time and at the same time maintain the calculation accuracy, a scheme having threshold limits given by 0.2 and 0.4 and $\Delta t = 0.02$, and with 15 568 cell numbers is adopted as the final computational scheme.

Table 1
The effect of mesh refinement and nondimensional time step ($\Delta t = Ut/D$) on the calculation results of the flow around a single cylinder at $Re = 200$

| Number of cells | $\Delta t$ | St | $\overline{C}_D$ | $C'_D$ | $C'_L$ |
|---|---|---|---|---|---|
| 25 999 | 0.02 | 0.200 | 1.364 | 0.033 | 0.426 |
| 24 186 | 0.01 | 0.201 | 1.360 | 0.030 | 0.473 |
| 15 568[a] | 0.02 | 0.196 | 1.320 | 0.026 | 0.426 |
| 8675 | 0.01 | 0.190 | 1.361 | 0.032 | 0.460 |

[a]The final chosen calculation scheme

Table 2
The calculated and measured results for the flow around a single cylinder

| Re | Investigators | St | $\overline{C}_D$ | $C'_D$ | $C'_L$ | $\overline{C}_{PB}$ | $C'_{PB}$ |
|---|---|---|---|---|---|---|---|
| **2-D simulation** | | | | | | | |
| 100 | Braza et al. (1986) | 0.160 | 1.34 | 0.036 | 0.19 | 0.6 | |
| | Kjellgren (1997) | 0.160 | 1.34 | 0.013 | 0.19 | | |
| | Su and Kang (1999) | 0.163 | 1.36 | 0.014 | 0.24 | 0.55 | |
| | Current work | 0.160 | 1.36 | 0.006 | 0.21 | 0.657 | 0.013 |
| 200 | Braza et al. (1986) | 0.200 | 1.35 | 0.071 | 0.55 | | |
| | Liu et al. (1998) | 0.192 | 1.35 | 0.035 | 0.49 | 0.956 | 0.095 |
| | Williamson and Browm (1998) | 0.197 | | | | | |
| | Farrant et al. (2000) | 0.196 | 1.36 | | 0.51 | | |
| | Meneghini et al. (2001) | 0.196 | 1.30 | 0.032 | 0.50 | | |
| | Current work | 0.196 | 1.32 | 0.026 | 0.426 | 0.920 | 0.092 |
| **3-D simulation** | | | | | | | |
| 300 | Kravchenko and Moin (1998) | 0.203 | 1.28 | | 0.40 | 1.01 | |
| | Persillon and Braza (1998) | 0.181 | 1.31 | | 0.254 | | |
| 200 | Zhang and Dalton (1998) | 0.198 | 1.32 | 0.041 | 0.43 | | |
| | Current work, $H/D = 16$ | 0.180 | 1.274 | 0.042 | 0.438 | 0.887 | 0.097 |
| **Experiments** | | | | | | | |
| 100 | Jordan and Fromm (1972) | 0.16–0.17 | 1.30 | | | | |
| 100 | Tanida et al. (1973) | | | | 0.03–0.09 | | |
| 100 | Friehe (1980) | 0.156–0.168 | | | | | |
| 200 | Williamson (1991) | 0.196 | | | | | |
| 720 | Norberg (1993, 2003) | 0.210 | 1.30 | | 0.11 | | 0.05 |

Although the vortex shedding phenomenon for a single cylinder occurs at $\mathrm{Re} > 40$, most experimental measurements of the fluctuating lift coefficient of the cylinder are only reported at Re greater than a few thousands. This is because the fluctuating pressure and force characteristics arising from vortex shedding are extremely difficult to measure experimentally at low Re. Norberg (2003) made an extensive review on previous experimental and numerical investigations concerning fluctuating lift acting on a single cylinder. However, it is obvious that experimental data on fluctuating force (lift and drag) is still lacking at low Re (Table 2). The presently calculated root-mean-square lift coefficient $C'_L$ is consistent with previous simulation results. However, there is a large difference with previous measured results (Tanida et al., 1973; Norberg, 1993, 2003). The difference may be due to two reasons. One is due to the difficulties associated with experimental measurement at low Re, and the other is due to cylinder random disturbance and the existence of vibrations in actual experiments which might be different from the specified simulation conditions. Since there is insufficient experimental data at low Re, it is difficult to identify clearly the reasons for the observed discrepancies. Therefore, it is beneficial to carry out more carefully designed experiments at low Re and performing numerical studies using higher precision and more accurate simulation method.

## 3. 2-D simulation results

The 2-D simulation can be regarded as flow over infinitely long cylinders. If 3-D effects at the ends of the cylinder are not significant, then the much more time-saving 2-D numerical simulation could reveal the basic flow physics and yield quantitative information which is extremely difficult to obtain experimentally. Numerical and experimental results could also complement and/or supplement each other in the investigation of complex flows around cylinder arrays.

Fig. 4. $\overline{C}_D$, $\overline{C}_L$ and St versus $L/D$ for four cylinders, in an in-line square configuration: experimental studies (Sayers, 1988, 1990; Lam anf Lo, 1992; Lam and Fang, 1995; Lam et al., 2003b); simulation studies (Farrant et al., 2000) and present results: (a) $\overline{C}_D$ of cylinders 1 and 2, (b) $\overline{C}_D$ of cylinders 3 and 4, (c) $\overline{C}_L$ of cylinders 1 and 2, (d) $\bar{C}_L$ of cylinders 3 and 4, (e) St of cylinders 1 and 2, (f) St of cylinders 3 and 4.

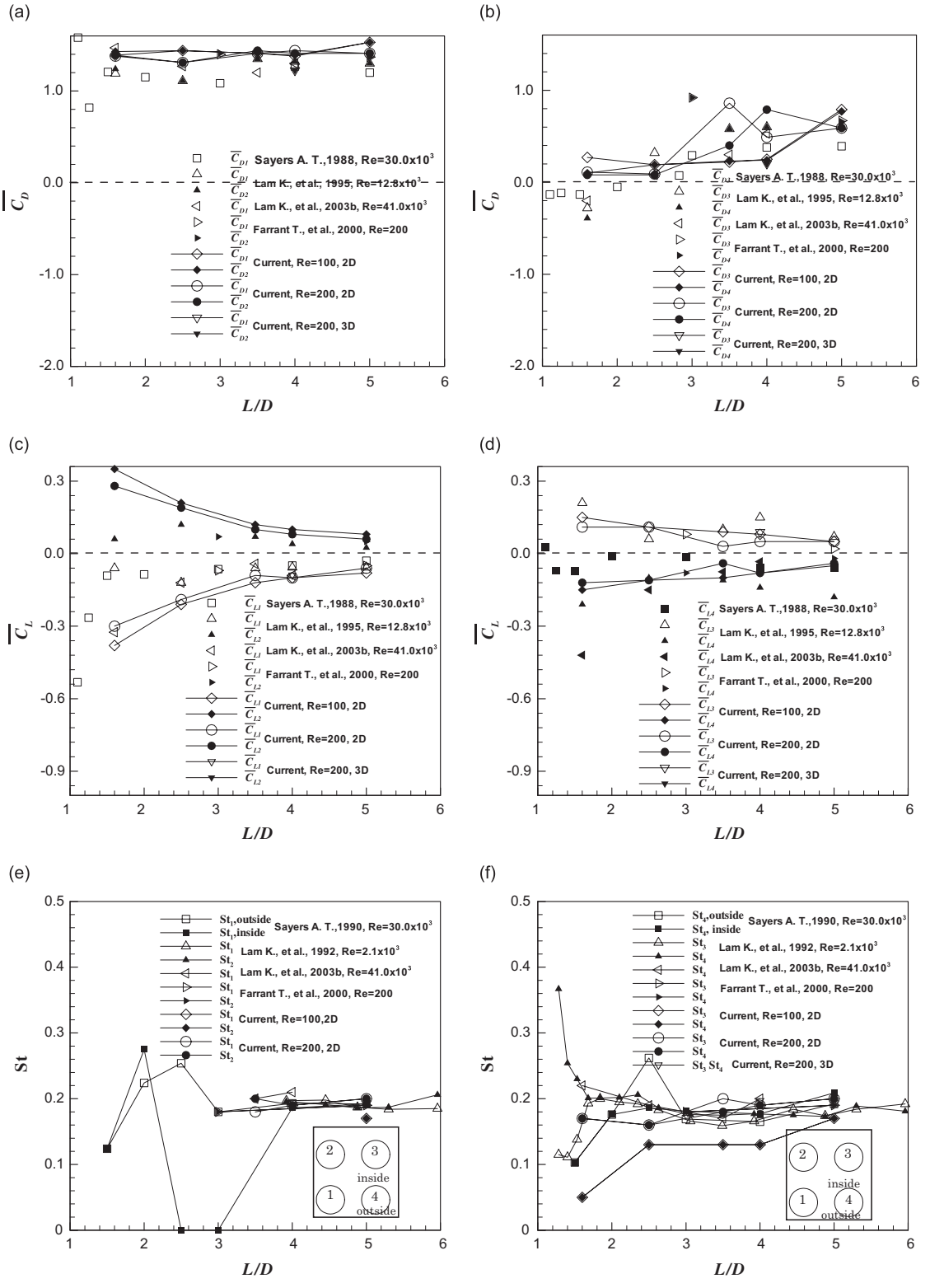
(a)
$\overline{C}_D$
L/D
$\overline{C}_{D1}$ Sayers A. T.,1988, Re=30.0x10^3
$\overline{C}_{D1}$ Lam K., et al., 1995, Re=12.8x10^3
$\overline{C}_{D2}$
$\overline{C}_{D1}$ Lam K., et al., 2003b, Re=41.0x10^3
$\overline{C}_{D1}$ Farrant T., et al., 2000, Re=200
$\overline{C}_{D2}$
$\overline{C}_{D1}$ Current, Re=100, 2D
$\overline{C}_{D2}$
$\overline{C}_{D1}$ Current, Re=200, 2D
$\overline{C}_{D2}$
$\overline{C}_{D1}$ Current, Re=200, 3D
$\overline{C}_{D2}$
(b)
$\overline{C}_D$
L/D
$\overline{C}_{D3}$ Sayers A. T.,1988, Re=30.0x10^3
$\overline{C}_{D4}$
$\overline{C}_{D3}$ Lam K., et al., 1995, Re=12.8x10^3
$\overline{C}_{D4}$
$\overline{C}_{D3}$ Lam K., et al., 2003b, Re=41.0x10^3
$\overline{C}_{D3}$ Farrant T., et al., 2000, Re=200
$\overline{C}_{D4}$
$\overline{C}_{D3}$ Current, Re=100, 2D
$\overline{C}_{D4}$
$\overline{C}_{D3}$ Current, Re=200, 2D
$\overline{C}_{D4}$
$\overline{C}_{D3}$ Current, Re=200, 3D
$\overline{C}_{D4}$
(c)
$\overline{C}_L$
L/D
$\overline{C}_{L1}$ Sayers A. T.,1988, Re=30.0x10^3
$\overline{C}_{L1}$ Lam K., et al., 1995, Re=12.8x10^3
$\overline{C}_{L2}$
$\overline{C}_{L1}$ Lam K., et al., 2003b, Re=41.0x10^3
$\overline{C}_{L1}$ Farrant T., et al., 2000, Re=200
$\overline{C}_{L2}$
$\overline{C}_{L1}$ Current, Re=100, 2D
$\overline{C}_{L2}$
$\overline{C}_{L1}$ Current, Re=200, 2D
$\overline{C}_{L2}$
$\overline{C}_{L1}$ Current, Re=200, 3D
$\overline{C}_{L2}$
(d)
$\overline{C}_L$
L/D
$\overline{C}_{L4}$ Sayers A. T.,1988, Re=30.0x10^3
$\overline{C}_{L3}$ Lam K., et al., 1995, Re=12.8x10^3
$\overline{C}_{L4}$
$\overline{C}_{L4}$ Lam K., et al., 2003b, Re=41.0x10^3
$\overline{C}_{L3}$ Farrant T., et al., 2000, Re=200
$\overline{C}_{L4}$
$\overline{C}_{L3}$ Current, Re=100, 2D
$\overline{C}_{L4}$
$\overline{C}_{L3}$ Current, Re=200, 2D
$\overline{C}_{L4}$
$\overline{C}_{L3}$ Current, Re=200, 3D
$\overline{C}_{L4}$
(e)
St
L/D
St1,outside St1,inside Sayers A. T.,1990, Re=30.0x10^3
St1 St2 Lam K., et al., 1992, Re=2.1x10^3
St1 St2 Lam K., et al., 2003b, Re=41.0x10^3
St1 St2 Farrant T., et al., 2000, Re=200
St1 St2 Current, Re=100,2D
St1 St2 Current, Re=200, 2D
2 3 inside 1 4 outside
(f)
St
L/D
St3,outside St3, inside Sayers A. T.,1990, Re=30.0x10^3
St3 St4 Lam K., et al., 1992, Re=2.1x10^3
St3 St4 Lam K., et al., 2003b, Re=41.0x10^3
St3 St4 Farrant T., et al., 2000, Re=200
St3 St4 Current, Re=100, 2D
St3 St4 Current, Re=200, 2D
St3 St4 Current, Re=200, 3D
2 3 inside 1 4 outside

### 3.1. Drag and lift coefficients and Strouhal number

The force vector on the cylinder surface is defined as

$$\mathbf{F} = \int_S \mathrm{d}\mathbf{F}_{\text{viscous}} + \int_S \mathrm{d}\mathbf{F}_{\text{pressure}}, \tag{3}$$

where $\mathbf{F}_{\text{viscous}}$ and $\mathbf{F}_{\text{pressure}}$, respectively, represent the contributions of viscous and pressure force. The force coefficient can then be defined as

$$\mathbf{C} = \frac{1}{\frac{1}{2}\rho U_\infty^2 D} \int_0^{2\pi} \mathbf{F} \cos\theta \, \mathrm{d}\theta. \tag{4}$$

Thus defined, the normal component of $\mathbf{C}$ to the oncoming flow direction is the instantaneous lift coefficient $C_L$, the parallel component of $\mathbf{C}$ to the flow direction is the instantaneous drag coefficient $C_D$.

Fig. 4 shows the results obtained by others and the present investigations for the flow around four cylinders in an in-line square configuration. Sayers first measured $\overline{C}_D$ and $\overline{C}_L$ by integrating the measured surface pressure (Sayers, 1988) where the contribution from the viscous force was not considered, and St by hot-wire anemometry technique (Sayers, 1990) at $\mathrm{Re} = 30.0 \times 10^3$. Sayers (1990) gave two values of St for each cylinder by measuring in the inner and outer side of the downstream cylinder, as shown in Fig. 4(e) and (f). Lam and Lo (1992) measured St at $\mathrm{Re} = 2.1 \times 10^3$, while Lam and Fang (1995) measured $\overline{C}_D$ and $\overline{C}_L$ at $\mathrm{Re} = 12.8 \times 10^3$, using methods similar to those of Sayers (1988, 1990). On the other hand, Lam et al. (2003b) measured $\overline{C}_D$, $\overline{C}_L C'_D$ and $C'_L$ directly at $\mathrm{Re} = 41.0 \times 10^3$ using a load cell. Farrant et al. (2000) numerically simulated a similar problem at $\mathrm{Re} = 200$, and $L/D = 3.0$ and 5.0. It is believed that the measured force coefficients given by Lam et al. (2003b) using a high precision load cell technique could provide a reliable and accurate value for reference and for comparison with the present numerical simulation, bearing in mind the difference in Re.

In general, the mean lift coefficients of cylinders 1 and 2 are equal in magnitude and opposite in direction, so are those of cylinders 3 and 4. The mean drag coefficients of cylinders 1 and 2 are also close to each other, so are those of cylinders 3 and 4. Thus, the following discussion will mainly concentrate on cylinders 1 and 4. Several important characteristics can be summarized as follows:

(i) For the $\mathrm{Re} = 200$ case shown in Fig. 4(a), the variation of $\overline{C}_{D1}$ with $L/D$ has a concave characteristic for $L/D$ between 1.6 and 4.0, namely, a slight decrease in value from $L/D = 1.6$ to a minimum at around $L/D = 2.5$ and then rises again. Such feature also exists at higher Re, such as observed in Sayers (1988), Lam and Fang (1995) and Lam et al. (2003b). However, the bottom values in the concave curves as well as the corresponding $L/D$ values are different for different Re. This feature comes from the change of flow patterns around cylinders 1 and 4 when $L/D$ increases. When $L/D = 1.6$, cylinder 4 is mostly located in the wake of cylinder 1, so the drag mainly acts on the upstream cylinder 1 (Fig. 1(a)). When $L/D$ increases up to 2.5, the outside free shear layer from cylinder 1 reattaches onto cylinder 4 and parts of the drag is assigned to cylinder 4. Consequently, the drag on cylinder 1 decreases. Finally, when $L/D$ reaches 3.5–4.0, a critical flow pattern transformation occurs. Each cylinder withstands independently the oncoming flow, so the drag on cylinder 1 increases again. For the case of $\mathrm{Re} = 100$, a similar feature also exists while the concave bottom locates near $L/D = 4.0$. The above similarity in drag characteristics and their order of magnitude should reflect that the general flow patterns and their transformations should also have great similarity over the range of Re considered.

(ii) In Fig. 4(b), at $\mathrm{Re} = 200$, the computed $\overline{C}_{D3}$ and $\overline{C}_{D4}$ increase by 9.56 and 5.0 times, respectively, when the $L/D$ changes from 2.5 to 3.5. Such an abrupt increase is due to the flow pattern transformation which will be discussed in the subsequent section later. However, the case where $\overline{C}_{D4}$ differs from $\overline{C}_{D3}$ by 1.61–2.15 times at $L/D = 3.5$ and 4.0 could be attributed to the effect of a low cycle bistable wake flow behind the downstream cylinders. Similarly, for the $\mathrm{Re} = 100$ case, the $\overline{C}_{D4}$ increases by 3.21 times at $L/D = 4.0$–5.0; this means that the flow experiences a significant flow pattern transformation there. Another feature is that, at $L/D \leqslant 2.0$, $\overline{C}_{D4}$ as reported in Sayers (1988), Lam and Fang (1995) and Lam et al. (2003b) is negative, while the present results show that $\overline{C}_{D4}$ are still in the positive region. This might be explained by the fact that, at high Re, the free shear layers from cylinder 1, after shielding the roll up immediately behind cylinder 4, induce a strong backflow that produces a negative drag on cylinder 4. At low Re, the wake vortex is formed further away from the cylinder and the backflow strength is weaker. Thus it is not enough to induce a negative drag on cylinder 4. On the other hand, at $L/D = 3.5$ and 4.0, the $\overline{C}_D$ reported by Lam and Fang (1995) is very close to the computed mean drag for cylinders 3 and 4 at $\mathrm{Re} = 200$. The $\overline{C}_D$ reported in Sayers (1988) and Lam et al. (2003b) are lower than the computed mean value and are closer to the lower values of the calculated drag resulting from the bistable wake effect behind cylinders 3 and 4, thus giving rise to different values of $\overline{C}_{D3}$ and $\overline{C}_{D4}$.

(iii) Fig. 4(c) shows that $\overline{C}_{L1}$ approaches zero asymptotically as $L/D$ increases; this signifies the weakening of flow interference between the two rows of cylinders. As a whole, the trend is consistent with the results of Sayers (1988), and Lam and Fang (1995) and (2003b) even though there is a large difference in Re, and higher values of computed $\overline{C}_{L1}$. It seems that a flow pattern transformation has no significant influence on the mean $\overline{C}_{L1}$. Actually, at $L/D = 1.6$–2.0, the present $\overline{C}_{L1}$ has a large discrepancy from the values reported by Sayers (1988) and Lam and Fang (1995), but agree well with those given by Lam et al. (2003b). As mentioned earlier, Lam et al. (2003b) used a higher precision load cell to measure the force on the cylinder which could be a better reference than the methods of Sayers (1988) and Lam and Fang (1995), especially at low $L/D$. For example, the accuracy of the pressure taps in measuring cylinder surface pressure may drop near the inside separation points because interference among cylinders is very severe at low $L/D$.

(iv) In Fig. 4(d), the computed $\overline{C}_{L4}$ curve as a whole approaches zero asymptotically. However, in the flow pattern transformation region as discussed in Fig. 4(b), a moderate S-type feature can be seen which shows that the mean lift $\overline{C}_{L4}$ is closely related to flow pattern transformation. When $L/D$ varies from 2.5 to 3.5 at $\mathrm{Re} = 200$, $\overline{C}_{L3}$ and $\overline{C}_{L4}$ increase by 2.75 and 3.67 times, respectively. On the other hand, when $L/D \leqslant 1.6$, a large difference between the present results and those of Lam et al. (2003a), Sayers (1988) and Lam and Fang (1995) occurs in $\overline{C}_{L1}$ and $\overline{C}_{L4}$. But when $L/D \geqslant 2.5$ the trend of variation and the order of magnitude become consistent with each other, except for the $\overline{C}_{L4}$ reported by Lam and Fang (1995). The large discrepancy at low $L/D$ could be attributed to the effect of Re and the accuracy of the pressure integration method used in Sayers (1988) and Lam and Fang (1995). On the other hand, the large difference in $\overline{C}_{L4}$ between the present result and that in Lam et al. (2003a) could be attributed to a strong 3-D interference of the flow wake derived from the upstream cylinder end (Fig. 12).

(v) The results of Farrant et al. (2000) and the present 3-D simulation give $\overline{C}_D$ and $\overline{C}_L$ close to the present 2-D simulation. The 3-D calculated $\overline{C}_D$ is lower than the corresponding 2-D result. One of the reasons could be due to the effect of the end walls which are not present in the 2-D calculations.

(vi) In the present 2-D simulation, St is calculated only when vortex shedding occurs behind the cylinder. If there is no vortex shedding behind the upstream cylinders, St is not calculated. Hence, at $\mathrm{Re} = 200$ and $L/D$ less than 3.0, no $\mathrm{St}_1$ is reported (Fig. 4(e)). However, when $L/D$ increases to 3.5, vortex shedding occurs and $\mathrm{St}_1$ is about 0.19, which is close to that reported by Sayers (1988), Lam and Lo (1992), Lam et al. (2003b) and Farrant et al. (2000). Similarly, at $\mathrm{Re} = 100$ and $L/D = 5.0$ vortex shedding occurs, and $\mathrm{St}_1$ thus deduced is $\sim$0.17.

(vii) In Fig. 4(f), at $\mathrm{Re} = 200$, $\mathrm{St}_4$ as a whole is consistent with that reported by Sayers (1988), by Lam and Lo (1992), by Lam and Lo (2003b) and by Farrant et al. (2000). For $\mathrm{Re} = 100$, in the region of $L/D < 5.0$, the present $\mathrm{St}_4$ is lower than those reported previously, and when $L/D = 5.0$, the St has a noticeable increase to a value close to that reported in Lam and Lo (1992), resulting from the flow pattern transformation. If the case $\mathrm{Re} = 200$ with $L/D$ changes from 2.5 to 3.5 is critically analysed, a similar increase in St also exists corresponding to a flow pattern transformation. The 3-D simulation result gives a calculated St which is more accurate than that obtained at $\mathrm{Re} = 200$ and $L/D = 4.0$. The bistable feature behind the downstream cylinders means two different values of St for cylinders 3 and 4; sometimes these two values interchange with each other. In Lam and Lo (1992), the two St values at $L/D < 1.6$ are artificially prescribed for the cylinders. In the 2-D simulations, at $\mathrm{Re} = 200$ and $L/D = 3.5$, two different St are obtained; thus indicating a bistable flow and the result agrees well with that discussed in Fig. 4(b). However, at $L/D = 4.0$, only one St is obtained.

(viii) Although Re differs substantially in the investigations listed in Fig. 4, the values of $\overline{C}_D$, $\overline{C}_L$ and St do not vary much with Re but have the same order of magnitude. This suggests that the flow patterns and their transformation with $L/D$ exist over a wide range of Re and it is mainly responsible for the behaviour of $\overline{C}_D$, $\overline{C}_L$ and St.

In summary, the present 2-D investigation is consistent with previously reported (both numerically simulated and measured) results. Therefore, it is expected that the present calculations could shed some light on the relation between flow and force characteristics. Some significant features, especially the large change in $\overline{C}_{D3}$, $\overline{C}_{D4}$, $\overline{C}_{L3}$, $\overline{C}_{L4}$ and St with $L/D$, imply that a flow pattern transformation has occurred. The next section will focus on this aspect.

### 3.2. Flow pattern and force characteristics

Flow patterns play a major role in the behaviour of the pressure distribution around the cylinder. This is especially true for the instantaneous fluctuating pressure, which has a significant effect on the characteristic of the flow-induced forces. As shown in Fig. 5, the flow pattern characteristics are clearly illustrated by the vorticity distribution plots around the four cylinders. For each diagram in Fig. 5, only one instantaneous vorticity distribution is shown. In reality, vortex shedding behind the cylinder can be in-phase, anti-phase or with a phase difference and sometimes exhibiting bistable behaviour. Here, attention is focused on the flow pattern transformation among the cylinders.

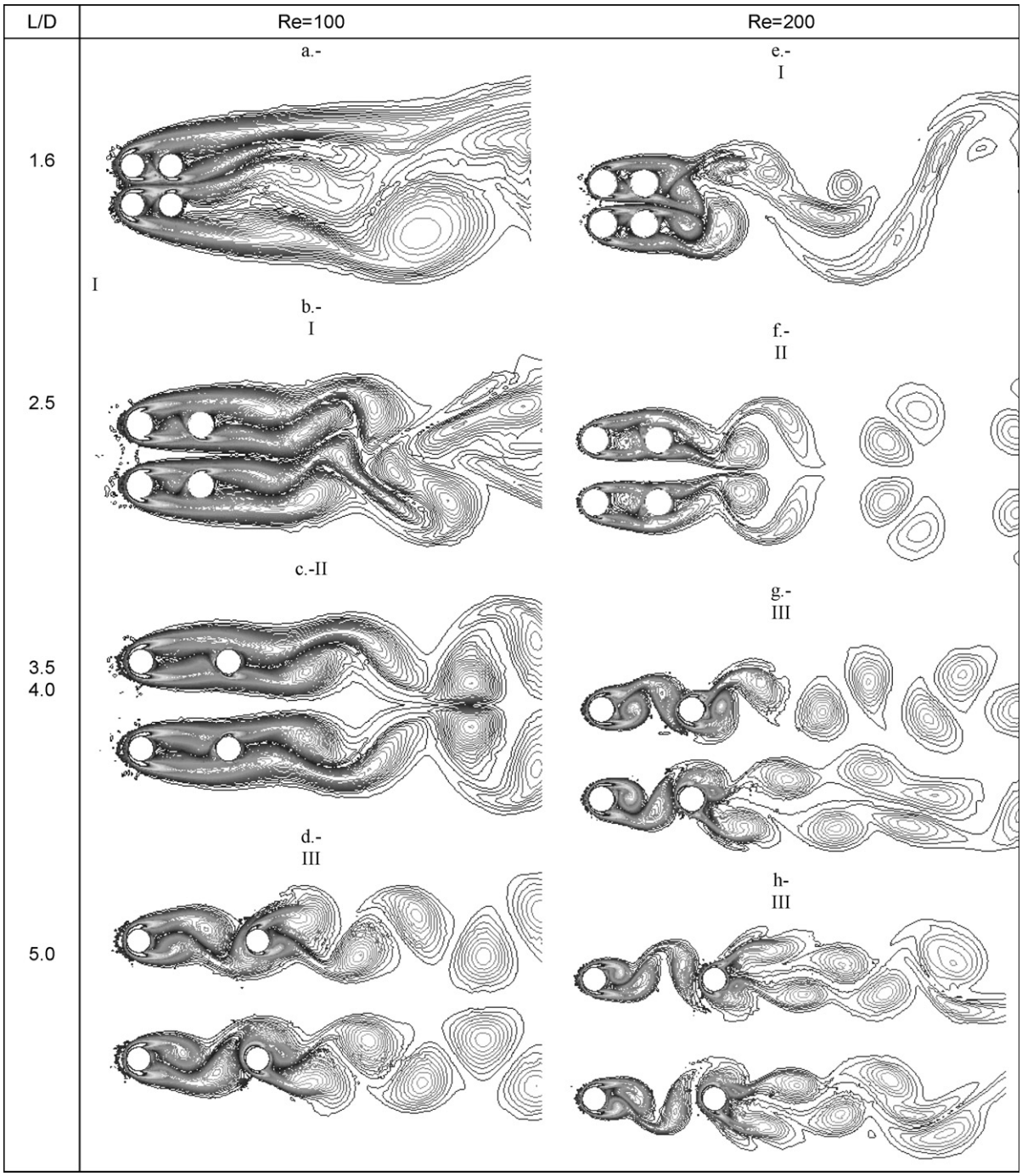


Fig. 5. Flow patterns (I)–(III), shown by vorticity distribution plots around four cylinders for 2-D simulation at Re = 100 and 200, and $L/D = 1.6$, 2.5, 3.5, 4.0 and 5.0.

In Figs. 5(a), (b) and (e), two inner side free shear layers from the upstream cylinders reattach onto the two downstream cylinder surfaces. However, the outside free shear layers do not reattach on the downstream cylinder surfaces. Instead, they engulf the downstream cylinders completely. Both inner and outer side free shear layers do not show significant wiggling. The flow pattern is almost steady during the whole process. This type of flow pattern is labelled as

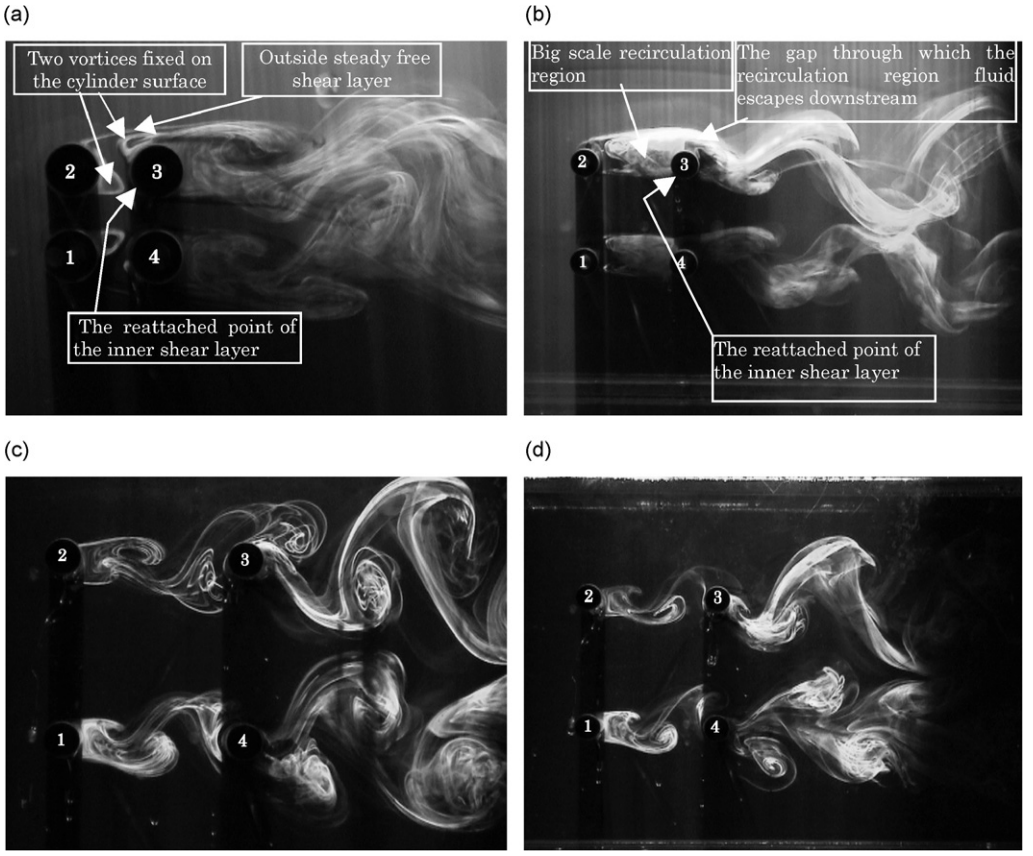


Fig. 6. Visualization at Re = 200. Solid blockage ratio is 15.4%. (a) $L/D = 1.6$; (b) $L/D = 3.5/4.0$; (c) $L/D = 5.0$, anti-phase shedding vortex; (d) $L/D = 5.0$, in-phase shedding vortex.

stable shielding flow pattern (I). The visualization picture at Re = 200 is shown in Fig. 6(a). The two fixed vortices on the cylinder surface is one of its significant features. In Figs. 5(c) and (f), the two inner side free shear layers reattach to the downstream cylinder surface while the outer side free shear layers do not. The outer side free shear layers are alternately wiggling near the downstream cylinders. This type of flow pattern is referred to as wiggling shielding flow pattern (II). The visualization result at Re = 200 is presented in Fig. 6(b). It can be seen that a large scale circulation region forms between cylinders 1 and 4. Such trapped large scale vortex escapes periodically downstream from the re-circulation region through the gap between cylinder 4 and the outer side free shear layer as shown in Fig. 6(b). In Figs. 5(d), (g) and (h), on the upstream cylinder the free shear layers roll up into mature vortices and then impinge on the downstream cylinder. This type of flow pattern is defined as vortex shedding flow pattern (III). The visualization pictures are shown in Figs. 6(c) and (d). Both anti-phase vortex shedding and in-phase vortex shedding occur intermittently. Critical $L/D$ can be defined to mark the transformation from one kind of flow pattern to another. However, it is believed that 2-D simulations would only be able to locate an approximate critical $L/D$ value.

The three definitions for the different flow patterns are consistent with the force characteristics on the cylinders. For the $\overline{C}_D$, $\overline{C}_L$, and St, as discussed in Fig. 4, a noticeable change often occurs when a flow pattern transformation occurs. For example, in Figs. 4(b) and (e), $\overline{C}_{D4}$ and $\mathrm{St}_1$ have a large change when $L/D$ varies from 2.5 to 3.5 at Re = 200 or from 4.0 to 5.0 at Re = 100. Here, the $L/D$ values at the corresponding Re are close to the critical value where the flow pattern transforms from (II) to (III).

In the 2-D simulation result shown in Fig. 7, $C'_D$ and $C'_L$ reflect the behaviour of the flow-induced unsteady force relative to the flow pattern transformation. At Re = 100, when the flow pattern changes from (I) to (II), although the curves do not appear to rise sharply due to the scaling effect in plotting the data in the same graph, $C'_D$ actually increases by 2.15 and 2.42 times for cylinder 1 (Figs. 7(a) and (b)) and cylinder 4, respectively, and $C'_L$ also has a 11.39

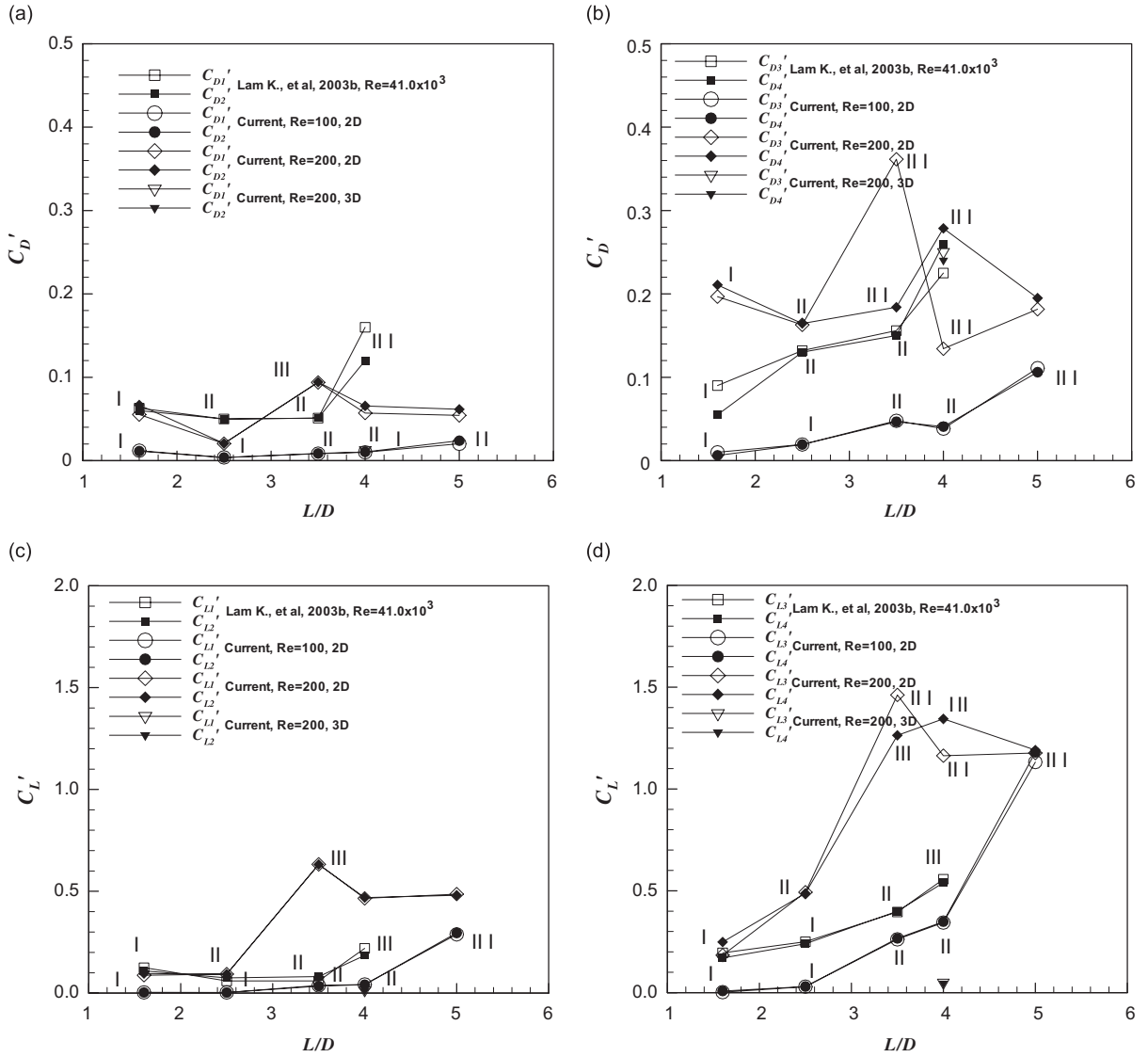


Fig. 7. $C'_D$ and $C'_L$ versus $L/D$ for four cylinders in an in-line square configuration: experimental result (Lam et al., 2003a,b); numerical simulations (present results with flow patterns (I)–(III); (a) $C'_D$ of cylinders 1 and 2, (b) $C'_D$ of cylinders 3 and 4, (c) $C'_L$ of cylinders 1 and 2 and (d) $C'_L$ of cylinders 3 and 4.

and 8.91 times increase (Figs. 7(c) and (d)). When the flow pattern changes from (II) to (III), $C'_D$ increases by 2.02–2.89 times, and $C'_L$ increases by 3.29–7.12 times. At Re = 200, when the flow pattern changes from (II) to (III), $\overline{C}_D$ increases by 2.22–4.60 times (Figs. 7(a) and (b)), and $C'_L$ increases by 2.59–6.77 times (Figs. 7(c) and (d)). At $L/D = 3.5$ and 4.0, $C'_{D3}$ and $C'_{D4}$ have a great difference, which is similar to the $\overline{C}_D$ characteristic at the same $L/D$ in Fig. 4(b). However, when the flow pattern changes from (I) to (II), $C'_D$ has a noticeable decrease. This can be understood from the previous discussion on Fig. 4(a) where $C'_D$ and $C'_L$ are basically consistent with those reported in Lam et al. (2003b). The present 3-D calculated flow result at Re = 200 shows a flow pattern (II) feature. Therefore, $C'_L$ and $C'_D$ on the upstream cylinders 1 and 2 are close to those given by flow pattern (II) of the corresponding 2-D calculations. However, $C'_L$ and $C'_D$ on the downstream cylinders 3 and 4 has a large discrepancy which may be due to the 3-D effect of the upstream cylinder end wake (Fig. 12). These results show that a flow pattern transformation is the main cause for the change in $\overline{C}_D$ and $\overline{C}_L$ or $C'_D$ and $C'_L$.

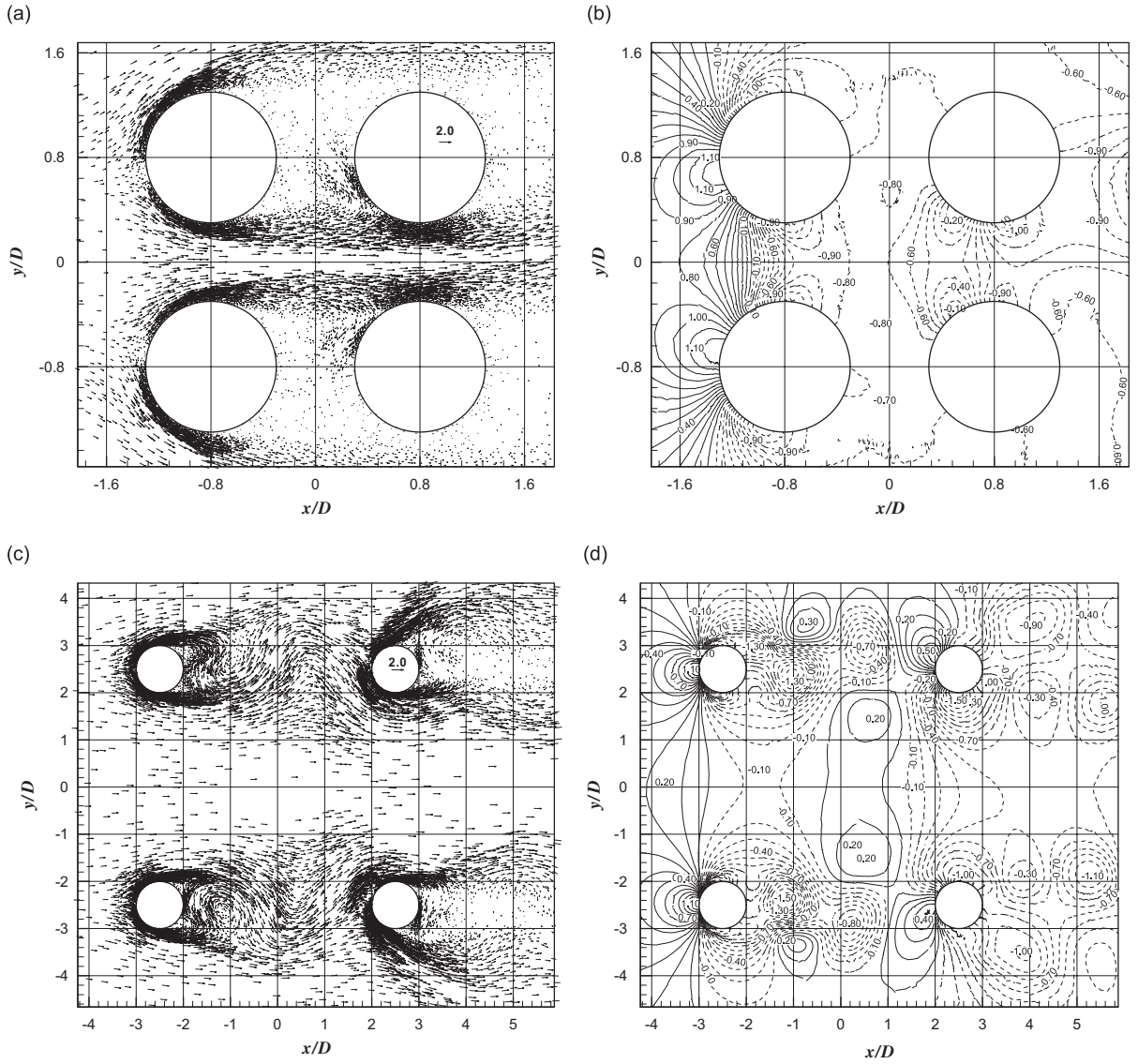


Fig. 8. (a, c) Velocity vector and (b, d) static pressure coefficient plots at an instantaneous time and Re = 200: velocity $u/U_\infty$, $v/U_\infty$ plots and pressure coefficient plots $C_p = (p - p_\infty)/(\frac{1}{2}\rho U_\infty^2)$; panels (a) and (b) for $L/D = 1.6$; panels (c) and (d) for $L/D = 5.0$. Solid lines are positive static pressure levels and dashed lines are negative. Minimum and incremental contour levels are, respectively, −1.6 and 0.1. Δ, Stagnation pressure points; ▼, flow separation points; ▲, flow reattachment points; ▽, vortex centres; □, minimum pressure points.

### 3.3. Pressure characteristics

It is well-known that, at high Re, the flow-induced force characteristics of the cylinder is mainly due to the pressure characteristics, and especially the fluctuating pressure characteristics resulting from vortex shedding. At high Re, the viscous effect is negligible. However, at low Re, viscous effects will increase. Braza et al. (1986) showed that at Re = 100 the mean viscous drag is about 0.34 and the mean pressure drag is about 1.03, while at Re = 200 the two values are 0.24 and 1.15, respectively. As for the lift force, viscous effects will further decrease relative to the pressure contribution. Bearing this in mind, the relation between the static pressure characteristics on the cylinder surface and the flow pattern transformation is discussed in this section.

The pressure coefficient on the cylinder surface is defined as

$$C_p = (p - p_\infty)/(\tfrac{1}{2}\rho U_\infty^2), \tag{5}$$

where $p_\infty$ is the oncoming flow static pressure and $p$ is the static pressure on the cylinder surface. Fig. 8 shows an instantaneous velocity vector and static pressure distribution for typical reattached (Figs. 8(a) and (b)) and impinging (Figs. 8(c) and (d)) flow patterns. They indicate that both the pressure stagnation and reattachment point are at the local highest pressure point on the cylinder surface, while the flow separation position, not being the lowest pressure point, has a lag angle relative to the lowest pressure point (Fig. 8(b)). On the other hand, when the impinging flow pattern occurs (Figs. 8(c) and (d)) the flow on the downstream cylinder becomes more complicated. The alternately shed vortices impinge and pass the downstream cylinder. Consequently, the stagnation pressure point occurs alternately on the opposite side of the cylinder (Figs. 8(c) and (d)). Here, the stagnation point still is the reattached point of a curved free shear flow, which can be clearly seen in Fig. 8(c). The most downstream separation point also has a lag angle to the lowest pressure position. Actually, these key flow points constantly move back and forth around a centre on the cylinder surface due to unsteady flow behaviour. If the pressure of the cylinder surface is averaged over 20 or more vortex shedding periods, these centres, namely the mean maximum or lowest pressure point, can be obtained. On the other hand, since the lowest pressure point is very close to the flow separation position (a small lag angle), it can easily be determined. For convenience, the lowest pressure point on the cylinder surface may be referred to as a measurement of the flow separation point. The following discussion will focus on the statistical mean value of the static pressure on the cylinder surface. The local mean maximum pressure position generally corresponds to the pressure stagnation or flow reattachment point, while the local mean lowest pressure point is a measurement of the flow separation position on the cylinder surface.

### 3.3.1. Mean static pressure coefficient

Figs. 9 and 10 show the time-mean static pressure distributions on the two upstream and two downstream cylinders, respectively. On the whole, the pressure distribution on cylinder 1 is a symmetry mapping of that on cylinder 2 about the point $\theta = 180^\circ$. The same is also true for cylinders 3 and 4. Therefore, in the next section, only the distributions on cylinders 1 and 4 are discussed.

The mean pressure distribution on the cylinder surface is calculated using the data in 20 periods. Thus, some lower frequency effect cannot be removed. For example, the slight asymmetry resulting from the bistable flow in the downstream wake does not disappear. Of course, if the number of periods used to deduce the average is large enough, the mean pressure distribution will become more symmetrical. Nevertheless, the slight asymmetry would not affect the analysis of the relation between the flow pattern and the pressure distribution.

*3.3.1.1. Pressure characteristics of the upstream cylinders.* Fig. 9 shows that, as $L/D$ increases, the stagnation point on cylinder 1 shifts from the inner side ($\theta = 15^\circ$) to the frontal position ($\theta = 0^\circ$). At $L/D = 1.6$, for $\mathrm{Re} = 100$ and 200, the stagnation point position is around $\theta = 15^\circ$ for cylinder 1. Lam and Fang (1995) determined experimentally that, at $L/D = 1.26$ and $\mathrm{Re} = 12.8 \times 10^3$, the stagnation point was at $\theta = 20^\circ$ for cylinder 1. This is consistent with the present result, in spite of the large difference in Re. The stagnation point shifting variation with $L/D$ also agrees with the conclusion drawn by Lam and Fang (1995); namely, if $L/D$ increases to 4.0, the stagnation point would shift to the frontal point of the cylinder ($\theta = 0^\circ$) and the pressure distribution would become similar to an isolated cylinder. This is the reason why the magnitude of the mean lift decreases when $L/D$ increases as shown in Fig. 4(c).

In Fig. 9, it can also be seen that the separation angle $\theta_s$ on cylinder 1 varies with $L/D$ and Re. At $\mathrm{Re} = 100$, $L/D = 1.6$, $\theta_s$ is estimated to be 101°, but when $L/D$ increases to 5.0 $\theta_s$ reduces to 88°, which means a net decrease of about 13°. In Lam and Fang (1995), $\theta_s$ changes from 85° to 70° when $L/D$ increases from 1.26 to 5.8 in the sub-critical Re range; giving a net decrease of 15°. Therefore, the $L/D$ variation from 1.6 to 5.0 has a significant influence on $\theta_s$ shifting by up to 13°. It also shows that, when $L/D$ increases, the interference between cylinders 1 and 2 decreases. On the other hand, a change of Re does not significantly affect the stagnation point position (Fig. 9), while it does obviously influence the position of the separation point at low $L/D$.

In the pressure recovery region behind the cylinders, the pressure coefficient varies from −0.75 to −1.6, and the curve becomes flat. Similar behaviour was also found in the studies of Lam and Fang (1995) whose results indicate that the pressure coefficient within the recovery region varies from −1.0 to −1.5.

*3.3.1.2. Pressure distributions on the downstream cylinders.* The mean static pressure distributions of cylinders 3 and 4 are shown in Fig. 10. At $\mathrm{Re} = 200$ and for $L/D$ values close to the critical spacing ratio (3.5 and 4.0), bistable flow often exists behind cylinders 3 and 4 with an alternate wide wake and a narrow wake. This bistable flow could be interpreted

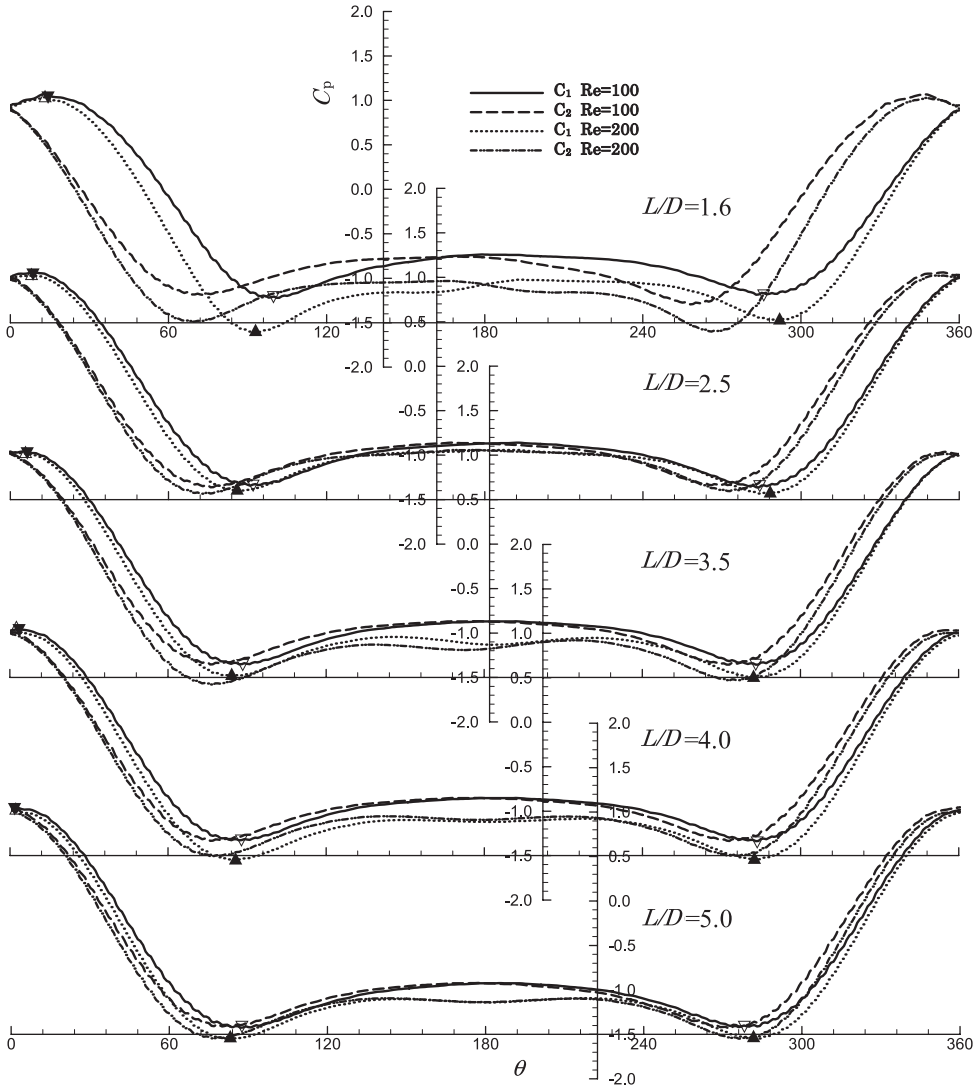


Fig. 9. Mean static pressure coefficient distribution on upstream cylinders 1 and 2; ▼ and Δ, stagnation pressure points; ▽ and ▲, lowest pressure points.

as a kind of lower frequency unsteady phenomenon in contrast to the vortex shedding frequency. On average, the static pressure is calculated over 20 cycles, so that the bistable low-frequency component will not be masked. At $L/D = 3.5$, the lowest pressure coefficient in the pressure recovery region corresponds to a wide bistable wake behind cylinder 3, while at $L/D = 4.0$ the bistable wide wake is behind cylinder 4. This is the reason why $\overline{C}_{D4}$ differs by 1.61–2.15 times with $\overline{C}_{D3}$ at $\mathrm{Re} = 200$, and $L/D = 3.5$ and 4.0 as shown in Fig. 4(b). If the averaging time is long enough, closer mirror image symmetry will be obtained. In other cases, except the critical bistable flow, symmetrical feature exists, and is similar to that reported by Lam and Fang (1995). Furthermore, in the pressure recovery region behind the downstream cylinders of flow patterns (I)–(III), all pressure coefficients are about −0.75 to −0.85 if the bistable effect is neglected. Therefore, a flow pattern transformation has no evident influence on the mean pressure recovery behind the downstream cylinders.

At $\mathrm{Re} = 100$ with $L/D$ varying from 1.6 to 4.0, and at $\mathrm{Re} = 200$ with $L/D = 1.6$ and 2.5, the location $\theta_m$ of maximum pressure coefficient on cylinder 4 varies in the range of 55–46°. The angle seems to decrease continuously with increasing $L/D$. Here, the maximum pressure coefficient is about −0.3 [−0.6 for high Re in Lam and Fang (1995)]. This shows that a flow pattern change from (I) to (II) has no significant effect on the maximum pressure coefficient and its position

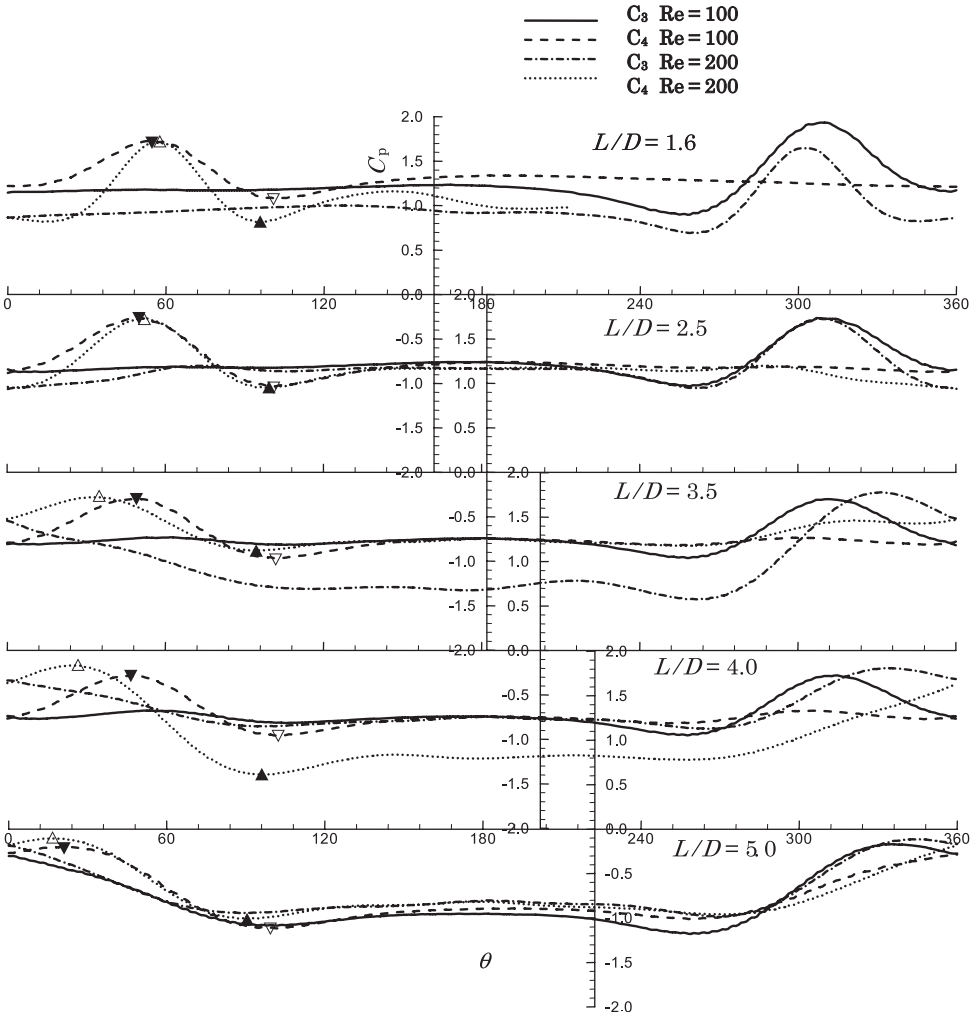


Fig. 10. Mean static pressure coefficient distribution on downstream cylinders 3 and 4: ▼ and Δ, stagnation pressure points; ▽ and ▲, lowest pressure points.

on the downstream cylinder. The position $\theta_m$ associated with flow patterns (I) and (II) seems to be mainly dependent on $L/D$.

If the conditions are changed to Re = 100 and $L/D$ varying from 4.0 to 5.0, and Re = 200 and $L/D$ varying from 2.5 to 3.5, $\theta_m$ decreases rapidly by approximately 14° and 25°, respectively. The maximum pressure coefficient in this $\theta_m$ range varies from −0.3 to −0.15. The main reason for this shift of $\theta_m$ is due to a change of the flow pattern from (II) to (III); namely, a transformation from a shear layer reattached flow to a vortex impingement flow. This change also causes $\overline{C}_{D4}$ to increase rapidly and $\overline{C}_{L4}$ to decrease when $L/D$ varying from 2.5 to 3.5, as shown in Fig. 4. Finally, for flow pattern (III), $\theta_m$ again seems to decrease continuously as $L/D$ increases.

According to Lam and Fang (1995), at $L/D \leqslant 2.48$, $\theta_m$ is about 55° for cylinder 4 which is close to the present result of 55–46° for flow patterns (I) and (II). At $L/D = 5.8$, $\theta_m$ decreases rapidly to 22° (Lam and Fang, 1995), corresponding to the vortex impingement case which is similar to a flow pattern transformation from (II) to (III) with $\theta_m$ decreases to 14–25°. Furthermore, although the pressure distribution curves in the pressure recovery region of cylinders 3 and 4 are not the same due to the presence of a bistable flow, $\theta_m$ is approximately symmetrical. The presence of the bistable flow does not seem to affect the maximum pressure position.

Therefore, it can be concluded that a change of the flow pattern does have a significant influence on the mean pressure distributions on the downstream cylinders. On the other hand, a change in the flow pattern has a weaker effect on the pressure distributions of the upstream cylinders.

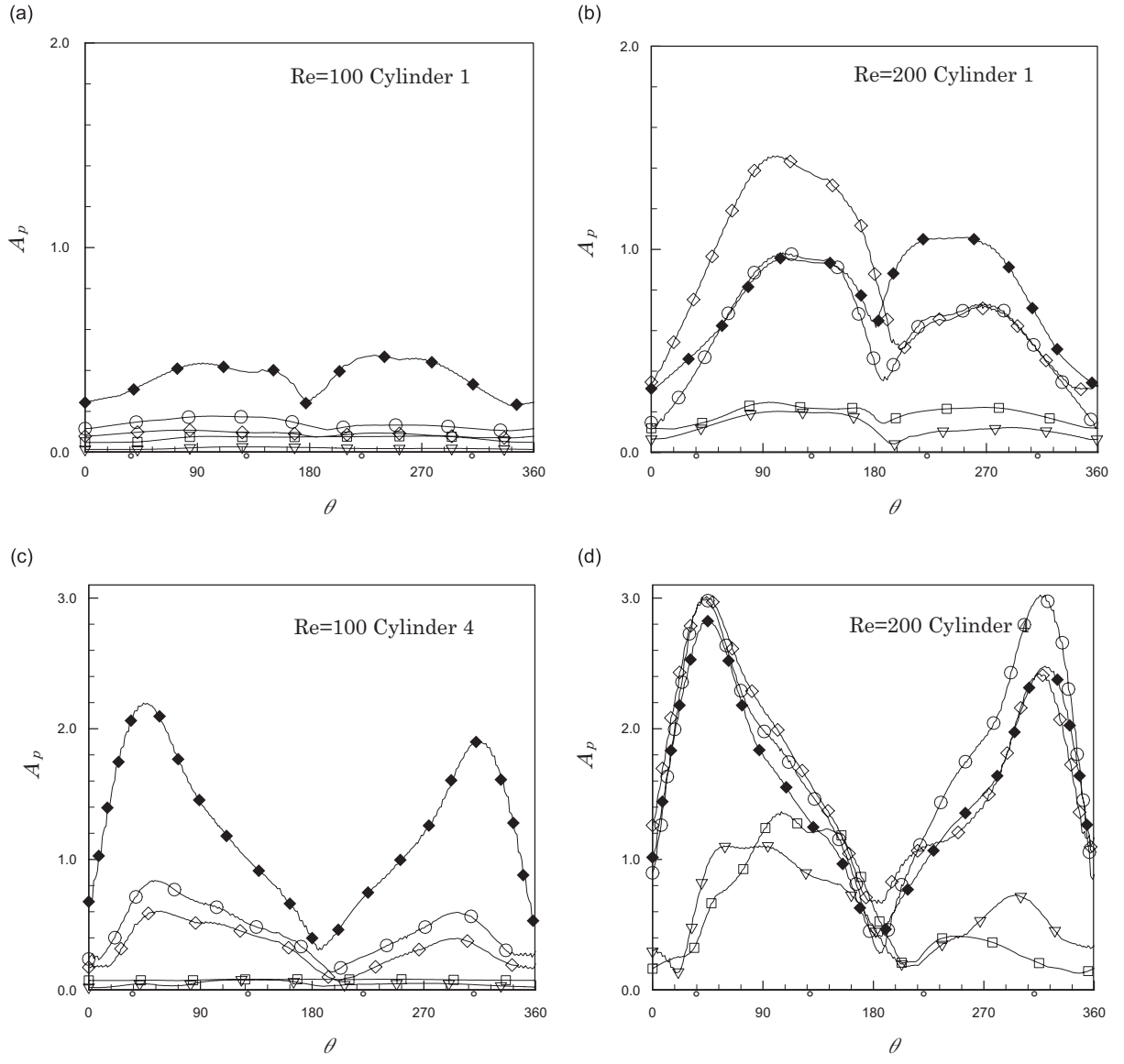


Fig. 11. Amplitude of fluctuating pressure coefficient on cylinder surfaces: □, $L/D = 1.6$; ▽, $L/D = 2.5$; ◇, $L/D = 3.5$; ○, $L/D = 4.0$; ◆, $L/D = 5.0$.

*3.3.2. Fluctuating pressure*

The amplitude $A_p$ of the fluctuating pressure coefficient induced by the vortex shedding on the cylinder is defined as

$$A_p(\theta) = \frac{1}{n}\sum_{i=1}^{n}\frac{1}{2}[(C_{p,\max,i}(\theta) - C_{p,\min,i}(\theta)], \tag{6}$$

where $C_{p,\max,i}$ and $C_{p,\min,i}$ is the maximum and minimum value of the pressure coefficient in the $i$th cycle, respectively; $n$ is the total number of cycles ($n = 20$ is chosen for the present study). A plot of $A_p$ at different $L/D$s is shown in Fig. 11.

The $A_p$ distribution on cylinder 2 is nearly a mirror image of that on cylinder 1. This is also the case for cylinders 3 and 4. The following discussion will again focus on cylinders 1 and 4, similar to that given above. On each cylinder, there exist two peak regions of pressure distribution on opposite sides of $\theta_m$ between 0° and 180° as shown in Fig. 11. The two peaks of $A_p$ appear in an alternate mode, i.e., if on one side of the cylinder the peak is positive, then on the other side the peak is negative, and *vice versa*.

*3.3.2.1. Fluctuating pressure characteristics on the upstream cylinder.* In Fig. 11(a), at $Re = 100$, the fluctuating pressure amplitude at $L/D = 1.6$ is larger than that at $L/D = 2.5$; the corresponding $C'_{D1}$ in Fig. 7(a) is also bigger. This is because at $L/D = 1.6$, the free shear layers from cylinder 1 almost embrace the whole downstream cylinder. Consequently, the fluctuating drag arising from vortex-induced force is mainly felt by cylinder 1. When $L/D$ increases to 2.5, the shielded region on the downstream cylinder shrinks. As a result, the downstream cylinder begins to burden more and more of the fluctuating drag; therefore, the fluctuating pressure amplitude and $C'_{D1}$ on the upstream cylinder decrease. On the other hand, $C'_{L1}$ almost has no change in the $L/D$ range of 1.6–2.5 because the shear flow around cylinder 1 does not cause any fluctuation in the $y$-direction. In general, the amplitude $A_p$ of the fluctuating pressure coefficients at $L/D$ ranging from 1.6 to 2.5 are all very low.

At $L/D = 3.5$, the flow pattern changes from (I) to (II). The fluctuating pressure amplitude on cylinder 1 (Fig. 11(a)) shows further increases. This leads to 2.15 times rise in $C'_{D1}$ and an even bigger rise of 11.39 times in $C'_{L1}$ (Fig. 7). The main reason is that the shear flow causes a stronger fluctuation in the $y$-direction in flow pattern (II), which results in the pressure amplitude increase in Fig. 11(a).

At $L/D = 5.0$, the flow pattern transits from (II) to (III). The fluctuating pressure amplitude on cylinder 1 as shown in Fig. 11(a) further increases; consequently, $C'_{D1}$ rises by 2.02 times and $C'_{L1}$ by 6.81 times (Fig. 7). The main reason for this is that vortex shedding occurs behind the upstream cylinder and this gives rise to a pressure amplitude increase as shown in Fig. 11(a). At $Re = 200$ (Fig. 11(b)), the behaviour of the pressure amplitude of the upstream cylinder can be classified into two groups: $L/D = 1.6$, 2.5 and $L/D = 3.5$–5.0. For the same reason, $C'_{D1}$ rises by 4.60 times and $C'_{L1}$ by 6.77 times when a flow pattern transition from (II) to (III) occurs. When the flow pattern transits from (I) to (II), the $A_p$ decreases, which is the same with that in Fig. 11(a), but the $C'_{D1}$ in Fig. 7(b) increases, different with that in Fig. 7(a).

From Figs. 8, 9 and 11, it can be seen that $\theta_s$ on the upstream cylinder is near the edge (near 90° and 270°) of the high value region of $A_p$ shown in Figs. 11(a) and (b) for the three flow patterns.

*3.3.2.2. Fluctuating pressure characteristics on the downstream cylinder.* In Fig. 11(c), $Re = 100$, three different kinds of flow patterns are clearly responsible for the three different modes of fluctuating pressure distributions. For flow Pattern (I), $L/D = 1.6$ and 2.5, $A_p$ are small and the curves are flat; therefore, $C'_{D4}$ and $C'_{L4}$ in Fig. 7 are low compared to those given for flow pattern (II). For flow pattern (II), $L/D = 3.5$ and 4.0, the $A_p$ curves display sharp peak values which increase by 4–12 times and result in a $C'_{D4}$ increase of 2.42 times and a $C'_{L4}$ increase of 8.91 times (Fig. 7). For flow Pattern (III), at $L/D = 5.0$, the peak of the $A_p$ curve increases by at least 2.44 times, thus rendering the $C'_{D4}$ increase by 2.60 times and the $C'_{L4}$ increase by 3.39 times (Fig. 7). When $Re = 200$ (Fig. 11(d)), it is clear that flow patterns (II) and (III) are responsible for the different distinctive fluctuating pressure distributions. The asymmetrical behaviour in pressure distribution on two sides of cylinder 4 at $L/D = 1.6$ indicates that the free shear layer on the outer side passes and cover the downstream cylinder and reattachment occurs on the inner side of the downstream cylinder. As $L/D$ increases from 2.5 to 3.5, the peak of the $A_p$ curve increases by 2.47 times, leading to a $C'_{D4}$ increase of 1.12 times and a $C'_{L4}$ increase of 2.59 times (Fig. 7). Here it should be noted that the effect of the bistable flow causes $C'_{D3}$ to increase by 2.0 times compared with $C'_{D4}$ at $L/D = 3.5$ and 4.0.

## 4. Numerical results for the 3-D simulation

In general, the important factors determining flow pattern transition are Re, $L/D$ and $H/D$. When analysing the 2-D simulation results, attention is focused on the effect of Re and $L/D$ on flow pattern transition. The relationship between the flow-induced force behaviour and the pressure distribution characteristics is also analysed.

However, 2-D simulation implies that the cylinder length is infinite while the actual cylinder length is finite. Thus, the cylinder end walls might have some strong influence on flow pattern transition. The present visualization result at $H/D = 16$ shows that for $Re = 100$ and $L/D = 1.6$–5.0, as well as for $Re = 200$ and $L/D = 1.6$–2.5 or 5.0, the calculated flow pattern is in general consistent with the observed flow pattern. However, at the critical condition around $L/D = 3.5$–4.0 and $Re = 200$, the observed flow patterns shown in Figs. 6 and 12(a) ($H6,/D = 16$) are completely different from the 2-D simulated result shown in Fig. 5(g). The observed flow pattern is the reattached flow pattern (II), but in Fig. 5(g), the simulated flow pattern is the impinging flow pattern (III). This suggests that the 2-D simulation could not properly reflect the 3-D flow behaviour at critical spacing and low $L/D$ ratios. At these values of $L/D$, it is necessary to carry out full 3-D numerical calculations to account for the effects of the cylinder end walls.

Therefore, a 3-D simulation has been conducted at $L/D = 4.0$ and $Re = 200$. In Fig. 13, the flow pattern inferred from the $x$-velocity $u$ and $z$-vorticity $\omega_z$ distributions agrees well with the flow visualization results shown in Fig. 12. The end effect is clearly illustrated. In Fig. 14, the calculated $z$-velocity $w$ plots at different $z/D$ planes are

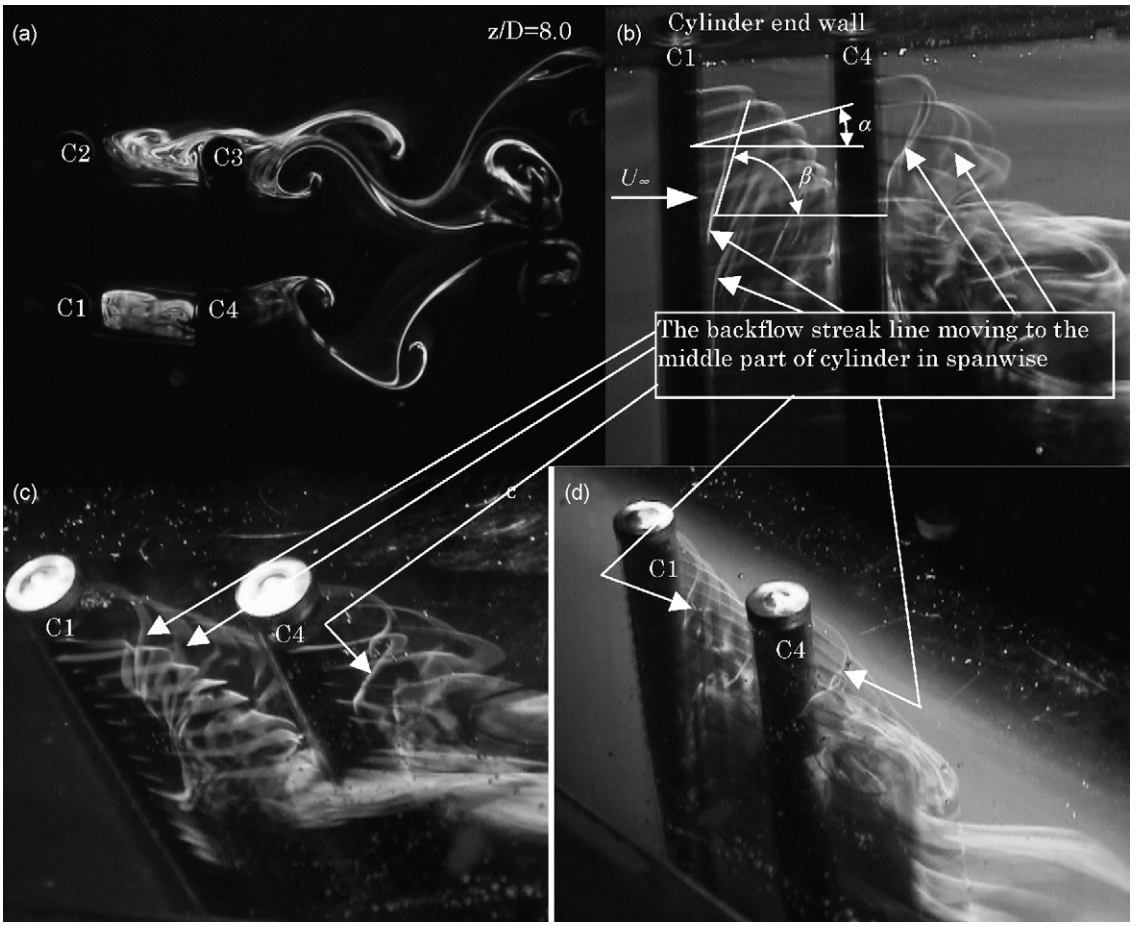


Fig. 12. Flow pattern at cylinder end observed by visualization at $L/D = 4.0$, $\mathrm{Re} = 200$ and $H/D = 16.0$. (a) Flow pattern in the cylinder middle plane, (b) view in the $y$-direction, (c) and (d) view in an oblique top direction. In (c) only the inside dye is illuminated; (b)–(d) show the backflow and no shedding vortex forming near the cylinder end plane.

shown. Around the cylinders there are positive and negative $w$ areas. A negative $w$ means the fluid flows towards the cylinder end plane and a positive $w$ denotes the opposite direction. It is well-known that the existence of the end wall often makes the flow to move away from the end wall surface, producing a positive $w$. Fig. 14 shows that the appearance of the cylinder end walls strengthens the positive $w$ region between the upstream and downstream cylinder and induces a weak negative $w$ outside the positive $w$ area. This is confirmed by the flow visualization result shown in Fig. 12. Firstly, in Fig. 12(b), the dyed streaklines, locating in the outside edge near the cylinder end, incline to the end wall and form an angle $\alpha$ with the $x$-direction. It indicates that the flow has a negative $w$ there directing to the cylinder end plane. Secondly, in the region between the upstream and downstream cylinders, the dye streakline alters its direction and moves upstream back to the cylinder mid-plane, forms an angle $\beta$ with the $x$-direction, and has a strong positive $w$ flow direction.

Therefore, it is evident that the flow has a strong 3-D characteristic at $H/D = 16$ and at critical spacing $L/D = 3.5$–$4.0$. These results can only be reproduced by a 3-D simulation rather than by a 2-D calculation. Further work using 3-D simulations is required for the clarification of the effects of cylinder aspect ratio on the flow characteristics.

## 5. Conclusions

The flow around four cylinders in an in-line square configuration is simulated using a finite-volume method and is also investigated using a flow visualization method. For the 2-D case, the simulations are carried out at $\mathrm{Re} = 100$ and

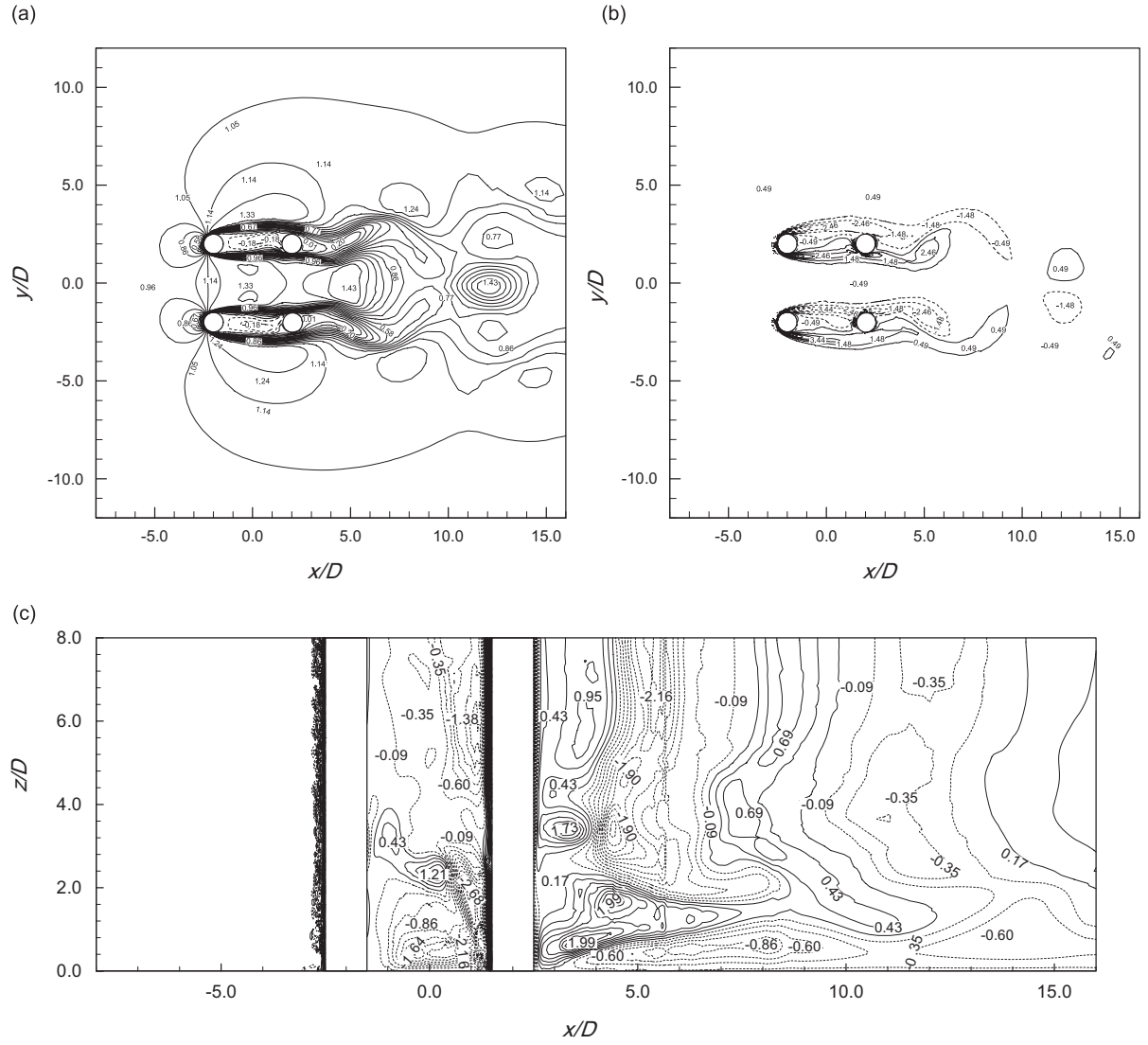


Fig. 13. Flow pattern in 3-D simulation at $L/D = 4.0$, $\mathrm{Re} = 200$. (a) $u/U_\infty$ at $z/D = 8.0$ plane, (b) $\omega_z D/U_\infty$ at $z/D = 8.0$ plane, (c) $\omega_z D/U_\infty$ at $y/D = -2.0$ plane. Solid lines are positive value levels and dashed lines are negative. Minimum and incremental contour levels are $-0.181$ and 0.095 for (a), $-30.89$ and 1.0164 for (b), $-3.455$ and 0.258 for (c), respectively.

200, and the spacing ratios $L/D$ are set at 1.6, 2.5, 3.5, 4.0 and 5.0. For the 3-D case, the simulation is only performed at $\mathrm{Re} = 200$, $L/D = 4.0$ and $H/D = 16$. The flow pattern dependence on Re, $L/D$ and $H/D$ is discussed. The relations between the flow pattern transition and the mean and fluctuating pressure characteristics on the cylinder surface, and the mean and fluctuating drag and lift behaviour are also discussed. The more significant results are summarized as follows.

(i) The calculated $\overline{C}_D$, $\overline{C}_L$, St and the flow pattern transformation are in agreement with previous results of the investigators. It shows that the 2-D numerical simulation can replicate the basic characteristics of the flow across the four cylinders in an in-line square configuration.

(ii) Three different flow patterns around the four cylinders are identified: (I) the outside free shear layer from the upstream cylinders shield the downstream cylinders completely, and do not wiggle in space; (II) the inner side and outer side free shear layers reattach to the downstream cylinder surface, and acutely wiggle in space; (III) the free shear layers from the upstream cylinders roll up into vortices and the vortices then impinge alternately on the downstream cylinder surfaces. A flow pattern transition from (I) to (II) or from (II) to (III) is the main reason for the observed jump change of $\overline{C}_D C'_D$ and $C'_L$.

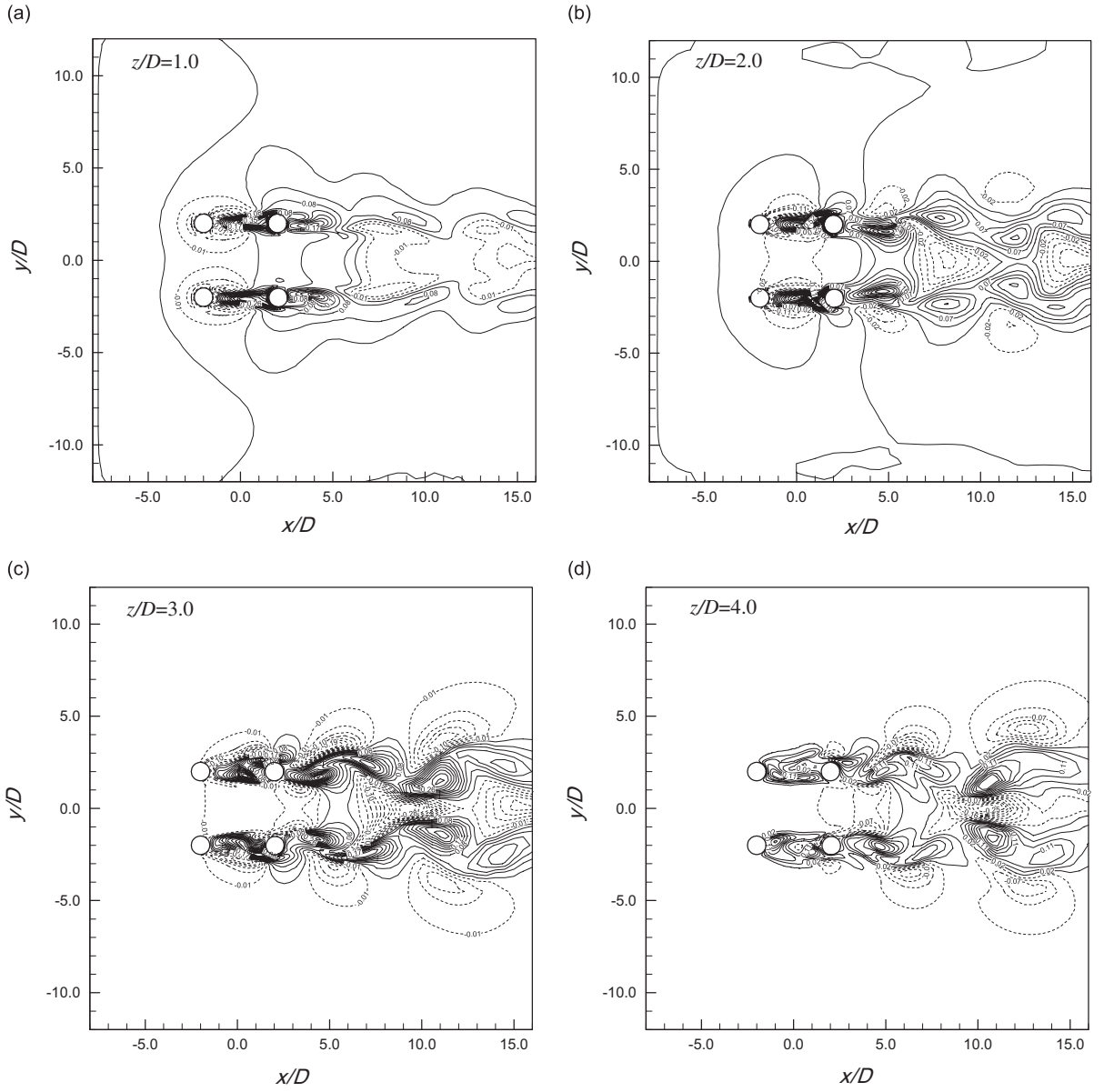


Fig. 14. $z$-Velocity ($w/U_\infty$) contour plots at different distance from cylinder end plane. Solid lines are positive value levels and dashed lines are negative. Incremental contour levels are 0.03. Minimum levels are −0.105, −0.112, −0.282 and −0.255 for (a), (b), (c) and (d), respectively.

(iii) The variation of $\overline{C}_D$ of the upstream cylinder with $L/D$ has a concave characteristic. The concave bottom is near $L/D = 2.5$–$3.0$ for $\mathrm{Re} = 200$ and 3.5–4.0 for $\mathrm{Re} = 100$. At $\mathrm{Re} = 100$, when the flow pattern changes from (II) to (III), $\overline{C}_D$ on the downstream cylinder increases by about 3.21 times. At $\mathrm{Re} = 200$, when the flow pattern changes from (II) to (III), $\overline{C}_D$ on the downstream cylinder increases by 5.0–9.56 times. However, $\overline{C}_L$ of the upstream cylinder approaches zero asymptotically as $L/D$ increases. At $\mathrm{Re} = 100$, when the flow pattern changes from (II) to (III), $\overline{C}_L$ on the downstream cylinder decreases linearly. At $\mathrm{Re} = 200$, when the flow pattern changes from (II) to (III), $\overline{C}_L$ on the downstream cylinder increases by 2.75–3.67 times.

(iv) At $\mathrm{Re} = 100$, when the flow pattern changes from (I) to (II), $C'_D$ of the four cylinders increases by 2.15–2.47 times, and $C'_L$ increases by 8.91–11.39 times. When the flow pattern changes from (II) to (III), $C'_D$ increases by 2.02–2.89

times, and $C'_L$ increases by 3.29–7.12 times. At Re = 200, when the flow pattern changes from (II) to (III), $C'_D$ increases by 2.22–4.60 times, and $C'_L$ increases by 2.59–6.77 times.

(v) The behaviour of mean pressure distribution on the cylinder determines the $\overline{C}_D$ and $\overline{C}_L$ characteristics. For example, a 15° shift of the pressure stagnation point will lead to a jump change of $\overline{C}_D$ and $\overline{C}_L$. The fluctuating pressure characteristics are also closely related to the $C'_D$ and $C'_L$.

(vi) The bistable wake flow behind the downstream cylinder mainly affects the $\overline{C}_D$ and the $C'_L$ of the downstream cylinders.

(vii) The dynamic and geometric parameters affecting the flow pattern are Re, $L/D$ and $H/D$. An increase or decrease of any of these parameters could lead to a flow pattern transition.

(viii) Flow pattern transition has an evident influence on the mean pressure distribution characteristics on the downstream cylinder, although it has little effect on the mean pressure distribution of the upstream cylinder.

(ix) At $H/D = 16$ and a critical $L/D$ of 3.5–4.0, the flow has strong 3-D characteristics; therefore, a 3-D simulation is required if the flow properties were to be resolved correctly.

## Acknowledgements

The authors wish to thank the Research Grants Council of the Hong Kong Special Administrative Region, China, for its support through Grant no. PolyU 5299/03E.

## References

Behr, M., Hastreiter, D., Mittal, S., Tezduyar, T.E., 1995. Incompressible flow past a circular cylinder: dependence of the computed flow field on the location of the lateral boundaries. Computer Methods in Applied Mechanics and Engineering 123, 309–316.

Braza, M., Chassaing, P., Ha Minh, H., 1986. Numerical study and physical analysis of the pressure and velocity fields in the near wake of a circular cylinder. Journal of Fluid Mechanics 165, 79–130.

Breuer, M., Bernsdorf, J., Zeiser, T., Durst, F., 2000. Accurate computations of the laminar flow past a square cylinder based on two different methods: lattice-Boltzmann and finite-volume. International Journal of Heat and Fluid Flow 21 (2), 186–196.

Connell S.D., Holmes D.G., Braaten M.E., 1993. Adaptive unstructured 2D Navier-Stokes solutions on mixed quadrilateral/triangular meshes. ASME Paper 93-GT-99.

Farrant, T., Tan, M., Price, W.G., 2000. A cell boundary element method applied to laminar vortex-shedding from arrays of cylinders in various arrangements. Journal of Fluids and Structures 14, 375–402.

Friehe, C.A., 1980. Vortex shedding from cylinders at low Reynolds numbers. Journal of Fluid Mechanics 100 (2), 237–241.

Jester, W., Kallinderis, Y., 2003. Numerical study of incompressible flow about fixed cylinder pairs. Journal of Fluids and Structures 17 (4), 561–577.

Jordan, F., Fromm, J., 1972. Oscillatory drag, lift and torque on a circular cylinder in a uniform flow. Physics of Fluids 15, 371.

Kjellgren, P., 1997. a semi-implicit fractional step finite element method for viscous incompressible flows. computational mechanics 20, 541–550.

Kravchenko, A.G., Moin, P., 1998. B-spline methods and zonal grids for numerical simulations of turbulent flows. Report No.TF-73, Flow Physics and Computational Division, Department of Mechanical Engineering, Stanford University, USA

Lam, K., Fang, X., 1995. The effect of interference of four equispaced cylinders in cross flow on pressure and force coefficients. Journal of Fluids and Structures 9, 195–214.

Lam, K., Lo, S.C., 1992. A visualization study of cross-flow around four cylinders in a square configuration. Journal of Fluids and Structures 6, 109–131.

Lam K., So R. M. C., Li J. Y., 2001a. Flow around four cylinders in a square configuration using surface vorticity method. In: Proceedings of the Second International Conference on Vortex Methods, Istanbul, Turkey.

Lam K., Li J.Y., Chan K. T., So R. M. C., 2001b. Velocity map and flow pattern of flow around four cylinders in a square configuration at low Reynolds number and large spacing ratio using particle image velocimetry. In: Proceedings of the Second International Conference on Vortex Methods, Istanbul, Turkey.

Lam K., Li J. Y., Chan K. T., So R. M. C., 2002. The flow patterns of cross flow around four cylinders in an in-line square configuration. In: The Tenth International Symposium on Flow Visualization, Kyoto, Japan.

Lam, K., Li, J.Y., Chan, K.T., So, R.M.C., 2003a. Flow pattern and velocity field distribution of cross-flow around four cylinders in a square configuration at low Reynolds number. Journal of Fluids and Structures 17, 665–679.

Lam, K., Li, J.Y., So, R.M.C., 2003b. Force coefficient and Strouhal numbers of four cylinders in cross flow. Journal of Fluids and Structures 18, 305–324.

Liu, C., Zheng, X., Sung, C.H., 1998. Preconditioned multigrid methods for unsteady incompressible flows. Journal of Computational Physics 139, 35–57.

Liu, Y., So, R.M.C., Lau, Y.L., Zhou, Y., 2001. Numerical studies of two side-by-side cylinders in a cross flow. Journal of Fluids and Structures 15, 1009–1030.

Meneghini, J.R., Saltara, F., Siqueira, C.L.R., Ferrari, J.J.A., 2001. Numerical simulation of flow interference between two circular cylinders in tandem and side-by-side arrangement. Journal of Fluids and Structures 15, 327–350.

Ni, M.J., Tao, W.Q., Wang, S.J., 1998. Stability-controllable second order difference scheme for convection term. Journal of Thermal Science 7 (2), 119–130.

Norberg, C., 1993. Pressure forces on a circular cylinder in cross flow. In: Eckelmann, H., Graham, J.M.R., Huerre, P., Monkewitz, P.A. (Eds.), Bluff-Body Wakes, Dynamics and Instabilities Proceedings of IUTAM Symposium, Göttingen, September 1992. Springer, Berlin, pp. 275–278.

Norberg, C., 2003. Fluctuating lift on a circular cylinder: review and new measurements. Journal of Fluids and Structures 17, 57–96.

Persillon, H., Braza, M., 1998. Physical analysis of the transition to turbulence in the wake of a circular cylinder by three-dimensional Navier–Stokes simulation. Journal of Fluid Mechanics 365, 23–88.

Sayers, A.T., 1988. Flow interference between four equispaced cylinders when subjected to a cross flow. Journal of Wind Engineering and Industrial Aerodynamics 31, 9–28.

Sayers, A.T., 1990. Vortex shedding from groups of three and four equispaced cylinders situated in cross-flow. Journal of Wind Engineering and Industrial Aerodynamics 34, 213–221.

Shyy, W., Thakur, S., Wright, J., 1992. Second order upwind and central difference schemes for recirculating flow computation. AIAA Journal 30, 923–932.

So, R.M.C., Liu, Y., Cui, Z.X., Zhang, C.H., Wang, X.Q., 2005. Three-dimensional wake effects on the flow-induced forces. Journal of Fluids and Structures 20, 373–402.

Su, M., Kang, Q., 1999. Large eddy simulation of the turbulent flowaround a circular cylinder at sub-critical Reynolds numbers. ACTA Mechanica Sinica 31, 100–105.

Tanida, Y., Okajima, A., Watanabe, Y., 1973. Stability of a circular cylinder oscillating in uniform flow or in a wake. Journal of Fluid Mechanics 61, 769–784.

Tezduyar, T.E., Shih, R., 1991. Numerical experiments on downstream boundary of flow past a cylinder. Journal of Engineering Mechanics 117, 854–871.

Williamson, C.H.K., 1991. 2-D and 3-D aspects of the wake of a cylinder, and their relation to wake computations. In: Anderson, C.R., Greengard, C. (Eds.), Vortex Dynamics and vortex Methods, Lectures in Applied Mathematics. American Mathematical Society, 28, Providence, QI, pp. 719–751.

Williamson, C.H.K., Browm, G.L., 1998. A series in $(1/\sqrt{\mathrm{Re}})$ to represent the Strouhal-Reynolds number relationship of the cylinder wake. Journal of Fluids and Structures 13, 1073–1085.

Zdravkovich, M.M., 1987. The effects of interference between circular cylinders in cross flow. Journal of Fluids and Structures 1, 235–261.

Zdravkovich, M.M., 2003. Flow around circular cylinders. Oxford University Press, Oxford.

Zhang, J., Dalton, C., 1998. A three-dimensional simulation of a steady approach flowpast a circular cylinder at low Reynolds number. International Journal of Numerical Methods in Fluids 26, 1003–1022.